O.V. Lounasmaa laboratory

Approaching the zero-temperature limit in superfluid dynamics and dissipation

---

Jaakko Hosio

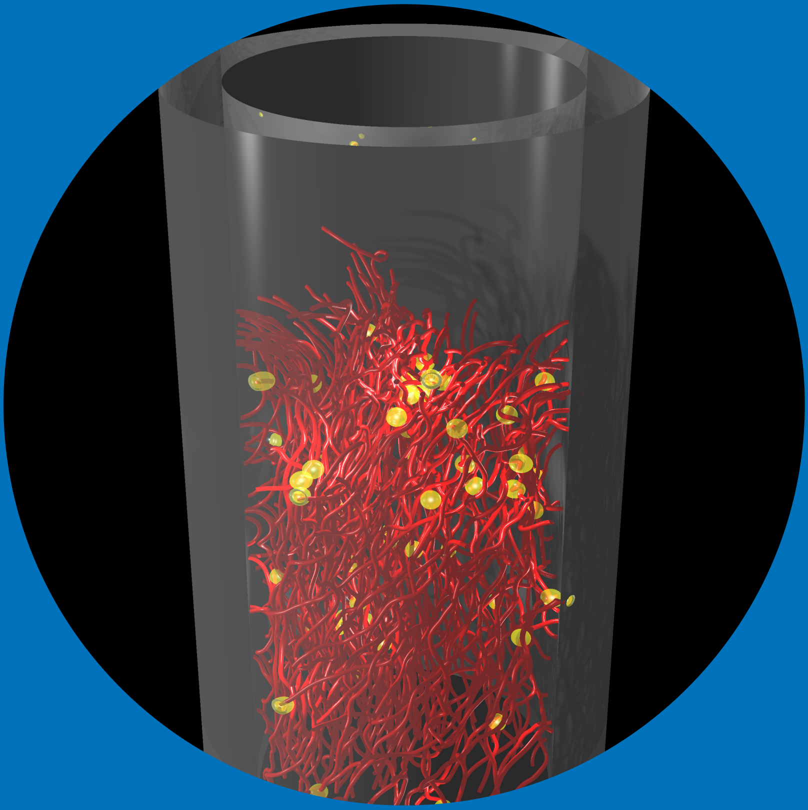

Aalto University

DOCTORAL DISSERTATIONS

Aalto University publication series
DOCTORAL DISSERTATIONS 145/2012

Approaching the zero-temperature limit in superfluid dynamics and dissipation

Jaakko Hosio

A doctoral dissertation completed for the degree of Doctor of Science (Technology) to be defended, with the permission of the Aalto University School of Science, at a public examination held at the lecture hall K216 of the school on 16 November 2012 at 12.

Aalto University
School of Science
O.V. Lounasmaa Laboratory
ROTA group

Supervising professor
Prof. Matti Kaivola

Thesis advisor
Dr. Vladimir Eltsov

Preliminary examiners
Prof. Edouard Sonin, The Hebrew University of Jerusalem, Israel
Dr. Viktor Tsepelin, The University of Lancaster, United Kingdom

Opponent
Prof. Andrei Golov, The University of Manchester, United Kingdom

Aalto University publication series
DOCTORAL DISSERTATIONS 145/2012

© Jaakko Hosio, front cover figure: Risto Hänninen

ISBN 978-952-60-4849-9 (printed)
ISBN 978-952-60-4850-5 (pdf)
ISSN-L 1799-4934
ISSN 1799-4934 (printed)
ISSN 1799-4942 (pdf)
http://urn.fi/URN:ISBN:978-952-60-4850-5

Unigrafia Oy
Helsinki 2012

Finland

441 697
Printed matter

Aalto University

Aalto University, P.O. Box 11000, FI-00076 Aalto www.aalto.fi

Abstract

Author
Jaakko Hosio

Name of the doctoral dissertation
Approaching the zero-temperature limit in superfluid dynamics and dissipation

Publisher School of Science

Unit O.V. Lounasmaa Laboratory

Series Aalto University publication series DOCTORAL DISSERTATIONS 145/2012

Field of research Experimental condensed matter physics

Manuscript submitted 7 August 2012 **Date of the defence** 16 November 2012

Permission to publish granted (date) 20 September 2012 **Language** English

☐ **Monograph** ☒ **Article dissertation (summary + original articles)**

Abstract

Most collective physical systems freeze and become immobile at zero temperature. Thus, there exist few systems where hydrodynamics can be experimentally studied in the zero-temperature limit. Most notable among these are the helium superfluids which remain in liquid state down to zero temperature and may support dissipationless superflow at sufficiently low flow velocities. The measurements of this thesis present the first information on the interplay of laminar and turbulent flow at higher velocities in the zero-temperature regime and the associated dissipation in these flow states. In contrast to earlier beliefs, the results show that there exist residual dissipation mechanisms in both cases which cause damping even in the zero-temperature limit.

A remarkable feature of superfluids is the quantization of flow through the creation of quantized vortex lines. These are formed at higher flow velocities, usually at some critical velocity. At higher temperatures the motion of vortices is damped by their interaction with the normal excitations, but this source of dissipation vanishes rapidly towards zero temperature. Thus, the motion of vortices should become dissipationless in the zero-temperature regime. However, as in viscous fluids, the smaller the dissipation the easier the flow is perturbed and becomes turbulent. Accordingly, vortex flow was expected to be turbulent in most experimentally achievable situations in the zero-temperature limit.

In this thesis superfluid dynamics is explored in a rotating ultra-low-temperature refrigerator with nuclear magnetic resonance and with measurements of Andreev scattering of ballistic quasiparticle excitations from quantized vortex lines in a cylindrical sample of superfluid helium-3. In an axially symmetric smooth-walled container, vortex flow turned out to be laminar, but perturbations, such as breaking the axial symmetry with obstacles or by changing the surface friction, was found to lead to turbulence. To stabilize laminar flow, the minimization of surface interactions is found to be of major importance. In spite of the sub-millikelvin temperatures, which are needed for the present studies, the advantage of superfluid helium-3 over the experimentally more accessible helium-4 superfluid is the more than two orders of magnitude larger vortex core diameter which reduces decisively disturbances in the flow of the vortex ends along solid walls.

Keywords hydrodynamics, helium-3, superfluid, quantized vortices, turbulent and laminar flow, dissipation

ISBN (printed) 978-952-60-4849-9 **ISBN (pdf)** 978-952-60-4850-5

ISSN-L 1799-4934 **ISSN (printed)** 1799-4934 **ISSN (pdf)** 1799-4942

Location of publisher Espoo **Location of printing** Espoo **Year** 2012

Pages 216 **urn** http://urn.fi/URN:ISBN:978-952-60-4850-5

A! **Aalto-yliopisto**

Aalto-yliopisto, PL 11000, 00076 Aalto www.aalto.fi

Tiivistelmä

Tekijä
Jaakko Hosio

Väitöskirjan nimi
Dynamiikka ja häviöt supranesteessä lähestyttäessä nollalämpötilarajaa

Julkaisija Perustieteiden korkeakoulu

Yksikkö O.V. Lounasmaa -laboratorio

Sarja Aalto University publication series DOCTORAL DISSERTATIONS 145/2012

Tutkimusala Kokeellinen materiaalifysiikka

Käsikirjoituksen pvm 07.08.2012 **Väitöspäivä** 16.11.2012

Julkaisuluvan myöntämispäivä 20.09.2012 **Kieli** Englanti

☐ **Monografia** ☒ **Yhdistelmäväitöskirja (yhteenveto-osa + erillisartikkelit)**

Tiivistelmä

Lähestulkoon kaikki fysikaaliset systeemit muuttuvat kiinteiksi lämpötilan laskiessa absoluuttiseen nollapisteeseen, ja niinpä hydrodynaamisia ilmiöitä nollalämpötilarajalla voidaan tutkia vain harvoissa erikoistapauksissa. Näistä merkittävimpiä ovat heliumsupranesteet, jotka säilyvät nestemäisenä aina nollalämpötilaan saakka ja jotka matalilla nopeuksilla kykenevät virtaamaan ilman virtausvastusta. Tässä työssä tutkitaan ensimmäistä kertaa laminaarisen ja turbulentin virtauksen vuorovaikutusta ja niihin liittyviä häviöitä lämpötilan nollarajalla. Toisin kuin aiemmin luultiin, molemmat virtausmuodot osoittautuivat häviöllisiksi aina nollalämpötilaan saakka.

Supranesteissä pyörivä virtaus esiintyy kvantittuneina virtauspyörteinä, joita kutsutaan vortekseiksi ja joita syntyy virtausnopeuden saavuttaessa tietyn kriittisen rajan. Kohtalaisen korkeissa supranestelämpötiloissa vorteksien liike määräytyy pitkälti vorteksiytimien vuorovaikutuksesta normaalineste-eksitaatioiden kanssa, mutta tämä vuorovaikutus heikkenee voimakkaasti lämpötilan laskiessa. Näin ollen vorteksien liikkeen tulisi muuttua häviöttömäksi nollalämpötilarajalla. Kuten viskooseissa nesteissä, virtaus kuitenkin muuttuu helposti turbulentiksi häviömekanismien heiketessä, ja niinpä turbulenssin odotettiin olevan merkittävässä osassa suurimmassa osassa kokeellisesti saavutettavissa olevissa tapauksissa nollalämpötilarajalla.

Tässä työssä supranestedynamiikkaa tutkitaan pyörivässä jäähdyttimessä ydinmagneettisen resonanssin ja termisten eksitaatioiden ns. Andreev-sironnan avulla helium-3-supranesteessä. Sileäseinäisen sylinterisymmetrisen näyteastian tapauksessa virtaus osoittautui käytännössä täysin laminaariseksi. Rikkomalla astian symmetriaa ja muuttamalla reunojen ominaisuuksia virtaus saatiin kuitenkin muuttumaan turbulentiksi. Helium-3-nesteen vorteksien ytimien suuri koko verrattuna helpommin tutkittavissa olevan helium-4-supranesteen vortekseihin havaittiin ratkaisevasti vähentävän virtaushäiriöitä kiinteään seinämään kiinnittyvissä vorteksien päissä. Tämän vuoksi helium-3-supraneste osoittautui erityisen hyödylliseksi nollalämpötiladynamiikan tutkimusalustaksi, vaikka sen tutkimiseen supranestenäyte joudutaankin jäähdyttämään alle millikelvinin lämpötilaan.

Avainsanat hydrodynamiikka, helium-3, supraneste, turbulenssi, kvantittunut virtauspyörre

ISBN (painettu) 978-952-60-4849-9 **ISBN (pdf)** 978-952-60-4850-5

ISSN-L 1799-4934 **ISSN (painettu)** 1799-4934 **ISSN (pdf)** 1799-4942

Julkaisupaikka Espoo **Painopaikka** Espoo **Vuosi** 2012

Sivumäärä 216 **urn** http://urn.fi/URN:ISBN:978-952-60-4850-5

Contents

Contents **i**

Acknowledgements **iii**

List of publications **v**

Author's contribution **vii**

1 Introduction **1**
- 1.1 Superfluidity of ^{3}He 2
- 1.2 Quantized vortices and rotating superfluid 5
- 1.3 Quantum turbulence 6

2 Experimental techniques **9**
- 2.1 Rotating cryostat and experimental setup 9
- 2.2 Quartz tuning fork oscillators 11
- 2.3 Nuclear-magnetic-resonance spectroscopy of ^{3}He 15

3 Experiments on superfluid dynamics in ^{3}He-B **19**
- 3.1 Propagation of thermal excitations in the presence of vortices . . 19
  - 3.1.1 Andreev scattering from a turbulent vortex tangle 20
  - 3.1.2 Quasiparticle scattering from a cluster of vortices 21
- 3.2 Laminar and turbulent flow responses to a change of rotation . . 25
  - 3.2.1 Dissipation of laminar vortex flow 27
  - 3.2.2 Spin-down response at the AB interface 29
  - 3.2.3 Quasiparticle-scattering measurements of vortex flow created in a spin-down to rest 32
- 3.3 Superfluid vortex front 36
  - 3.3.1 Thermal signal from dissipation of turbulence in the vortex front 38
  - 3.3.2 Front propagation in a decoupled superfluid 41

4 Summary and conclusions **45**

References **49**

Acknowledgements

The work described in this doctoral thesis was carried out in the ROTA group of the O.V. Lounasmaa Laboratory (former Low Temperature Laboratory). Writing the thesis would not have been possible without the help and support of the kind and skilled people around me, to only some of whom it is possible to extend particular attention here. I owe my sincere thanks to Professor Mikko Paalanen for hiring me in the spring of 2005 and to Professor Matti Krusius, the leader of our group until 2010, for his advice and devotion to the research I feel privileged to have been part of.

I cannot find words to express my gratitude to my instructor Vladimir Eltsov for his continuous professional guidance, encouragement, and patience. In addition to having been a pleasure to work with, he has taught me more about physics, both experimental and theoretical, than anyone else during the course of my studies. I owe my deepest gratitude to Rob de Graaf and Petri Heikkinen for their contributions in the experimental work and for sharing the responsibility for the operation of the cryostat. It was a pleasure to share an office with Petri and for some time with Jere Mäkinen, whom I also thank for collaboration. Numerical calculations on vortex dynamics by Risto Hänninen and theoretical work by Professor Grigori Volovik have been invaluable and are highly appreciated.

I have benefited greatly from our collaboration with many low-temperature research groups from abroad. I want to thank Rich Haley, Victor L'vov, Ladislav Skrbek, Wilfried Schoepe, Peter Skyba, and Paul Walmsley for their contributions to my work. My special thanks belong to David Schmoranzer for his contributions to our joint project during his two visits and for his friendship. I am also grateful to the fellow graduate students Heikki Junes, Matti Manninen, Elias Pentti, Juho Rysti, and Anssi Salmela for making the lab an inspiring and convivial place to work at.

I thank my supervising Professor Matti Kaivola for advice and taking care of the practical issues at the last stages of the graduation process and acknowledge the help of the technical and the administrative personnel of our laboratory. The support of my family has been invaluable and unconditional. Finally, I owe my deepest gratitude to my wife Noora for her love, support, and standing by me during the turbulent but warm times it took to prepare this thesis.

List of publications

This thesis consists of an overview and the following publications.

I R. Blaauwgeers, M. Blažkova, M. Človečko, V. B. Eltsov, R. de Graaf, J. Hosio, M. Krusius, D. Schmoranzer, W. Schoepe, L. Skrbek, P. Skyba, R. E. Solntsev, and D. E. Zmeev. *Tuning Fork: Thermometer, Pressure- and Viscometer for Helium Liquids*. Journal of Low Temperature Physics **146**, 537 (2007).

II M. Blažková, M. Človečko, V. B. Eltsov, E. Gažo, R. de Graaf, J. J. Hosio, M. Krusius, D. Schmoranzer, W. Schoepe, L. Skrbek, P. Skyba, R. E. Solntsev, W. F. Vinen. *Vibrating Quartz Fork - a Tool for Cryogenic Helium Research*. Journal of Low Temperature Physics **150**, 525 (2008).

III V. B. Eltsov, R. de Graaf, P. J. Heikkinen, J. J Hosio, R. Hänninen, M. Krusius and V. S. L'vov. *Stability and Dissipation of Laminar Vortex Flow in Superfluid* ^{3}*He-B*. Physical Review Letters **105**, 125301 (2010).

IV V. B. Eltsov, R. de Graaf, P. J. Heikkinen, J. J. Hosio, R. Hänninen, and M. Krusius. *Vortex Formation and Annihilation in Rotating Superfluid* ^{3}*He-B at Low Temperatures*. Journal of Low Temperature Physics **161**, 474 (2010).

V J. J. Hosio, V. B. Eltsov, R. de Graaf, P. J. Heikkinen, R. Hänninen, M. Krusius, V. S. L'vov, and G. E. Volovik. *Superfluid vortex front at* $T \to 0$*: Decoupling from the reference frame*. Physical Review Letters **107**, 135302 (2011).

VI P. M. Walmsley, V. B. Eltsov, P. J. Heikkinen, J. J Hosio, R. Hänninen, and M. Krusius. *Turbulent vortex flow responses at the AB interface in rotating superfluid* ^{3}*He-B*. Physical Review B **84**, 18453 (2011).

VII J. J. Hosio, V. B. Eltsov, R. de Graaf, M. Krusius, J. Mäkinen, and D. Schmoranzer. *Propagation of thermal excitations in a cluster of vortices in superfluid* ^{3}*He-B*. Physical Review B **84**, 224501 (2011).

VIII J. J. Hosio, V. B. Eltsov, M. Krusius, and J. T. Mäkinen. *Quasiparticle-scattering measurements of laminar and turbulent vortex flow in the spin-down of superfluid* ^{3}*He-B*. Physical Review B **85**, 224526 (2012).

IX J. J. Hosio, V. B. Eltsov, P. J. Heikkinen, M. Krusius, and V. S. L'vov. *Energy and angular-momentum balance in wall-bounded superfluid turbulence*. (arXiv:1208.2647) (2012).

X J. J. Hosio, V. B. Eltsov, and M. Krusius. *Thermal Detection of Turbulent and Laminar Dissipation in Vortex Front Motion*. Journal of Low Temperature Physics (2012), DOI: 10.1007/s10909-012-0709-1.

Throughout the overview, the publications will be referred to by their Roman numerals.

Author's contribution

The publications in this Thesis result from team work by the ROTA group at the Low Temperature Laboratory. I was responsible for the ^{4}He measurements in publication **I** as my first project as an undergraduate student. The measurements on Andreev reflection from turbulent vortex tangles in publication **II** were done and analyzed by me as a part of my undergraduate project.

I contributed to the reconstruction of the ROTA refrigerator after starting my graduate studies in the summer 2008 and participated in locating and removing the heat leaks to the ^{3}He-B sample. This reduced the heat leak by more than an order of magnitude and made the measurements of this thesis below $0.2\,T_\mathrm{c}$ possible. I had the main responsibility for designing, constructing, and installing the experimental cell used in the experiments whose results were published in **III**-**VIII** and **X**. I also prepared, tested, and installed the quartz oscillators used in **III**-**X**. My contribution in publications **III** and **IV** lies in participating in the completion of the measurements and in having a minor role in the data analysis.

During the experimental work over two and a half years, I shared the responsibility of the day-to-day operation of the rotating refrigerator with another graduate student. I had a significant role in the measurements and in the data analysis in **V**-**X**, of which **VII**-**X** are written by me. I also participated in the writing process of all the publications for which I was not the main responsible author by discussing and commenting on the manuscripts at different stages of their preparation and in some publications by preparing figures.

Chapter 1

Introduction

One of the most remarkable features of superfluids is the existence of quantized vortices as first suggested by Onsager [1]. The idea was further developed by Feynman [2] and demonstrated experimentally in superfluid ^{4}He by Vinen about half a century ago [3]. Vortices in superfluid ^{3}He were observed twenty years later in measurements performed in a rotating refrigerator [4, 5]. The motion of quantized vortices is of great interest and has been studied extensively during the past fifty years. Superfluid turbulence, the dynamics of a tangle of quantized vortex lines, has been studied for five decades in superfluid ^{4}He but only for about ten years in superfluid ^{3}He. The most recent frontier is the zero-temperature limit where the nature of superfluid dynamics is currently actively discussed.

This thesis deals with experiments on dynamic phenomena in ^{3}He superfluid. One of the main objectives of the work is to study what happens to fluid motion when temperature approaches the absolute zero. The focus is on the dissipation of the superfluid motion in the $T \to 0$ limit, where the effect of the conventional damping mechanisms strongly decreases. The interesting questions in this limit are what type of superfluid motion can be excited and how it evolves in time, is the motion dissipative or truly superfluid, and if it is dissipative, what are the dissipation mechanisms.

Superfluid ^{3}He offers a unique environment to study dissipative fluid motion. In ^{3}He superfluid the strength of the dissipative forces in experiments can be easily varied by many orders of magnitude by scanning the temperature. Unlike in classical viscous fluids or superfluid ^{4}He at finite temperatures, in ^{3}He-B the dynamics is concerned with identical singly quantized vortex lines with little complication from the presence of the very viscous normal component. The large size of the vortex cores in ^{3}He reduces the surface interactions in comparison to ^{4}He. Excellent measuring procedures are available for studying vortex densities and configurations: nuclear-magnetic-resonance methods and quasiparticle-beam techniques, both of which are utilized in this work. Entirely new types of vortex measurements, which have not been studied before, become possible in ^{3}He, such as the injection of seed vortices in vortex free flow in a container rotating at constant velocity.

Organization

The overview of the thesis is organized as follows: Section 1.1 briefly introduces some basic properties of superfluid ^{3}He and concepts relevant to the work presented. More comprehensive overviews can be found in Refs. [6, 7, 8, 9]. In Secs. 1.2 and 1.3, quantized vortices and their motion are discussed. Chapter 2 summarizes the experimental techniques and physical phenomena utilized in the experiments starting with a brief description of the rotating refrigerator and the experimental setup in Sec. 2.1. Section 2.2 introduces an important new experimental tool, an oscillating quartz tuning fork, whose use in cryogenic fluids was discussed in paper **I**. The results presented in Chap. 3 are divided in three categories: Sec. 3.1 presents studies on the dynamics of thermal excitations in the presence of quantized vortices published in papers **II** and **VII**. In Sec. 3.2, experiments on vortex dynamics after a change of rotation velocity are presented. These studies were discussed in papers **III**, **IV**, **VI**, and **VIII**. The results on our extensive studies on the turbulent superfluid vortex front, which were published in papers **V**, **IX**, and **X** are summarized in Sec. 3.3. Conclusions in Chap. 4 finish the overview.

1.1 Superfluidity of ^{3}He

At room temperature, helium is one of the least exciting elements: a colorless, odorless, and practically inert monatomic gas. Its best known application to general public is probably the filling of balloons. Helium is the second most abundant element in the Universe constituting 23% of its baryonic mass. Of the two stable isotopes, ^{3}He and ^{4}He, the latter is far more common: only a few ppm of the helium from natural gas sources is ^{3}He [10].

The low-temperature behavior of the helium isotopes is much more interesting as they have many unique properties only explained by the concepts of quantum mechanics. They liquify only below 5 K, at the lowest temperature of all elements, and neither ^{3}He nor ^{4}He solidify even at absolute zero unless a pressure of order 30 bar is applied. This unique property is a consequence of the large zero-point energy and weak inter-atomic forces binding the atoms in the liquid.

All particles fall into two classes depending on their spin. Those with integral spin, such as ^{4}He, are bosons, whereas those with half integral spin, such as ^{3}He, are fermions. Consequently, the two isotopes obey different quantum statistics, which leads to major differences in their low-temperature properties. Bosonic particles favor a large occupation of a single quantum state. Below a certain transition temperature a macroscopic number of bosons occupy the lowest energy state of the system. This so-called Bose-Einstein condensation (BEC) was observed in dilute gases of alkali atoms in 1995 [11, 12] and is believed to be the underlying mechanism for the superfluid transition in ^{4}He at temperature $T \approx 2$ K [13]. The condensed state of liquid ^{4}He below 2 K is called superfluid due to its unusual properties, such as the ability to support flow with no apparent dissipation.

In contrast, the Pauli exclusion principle forbids two identical fermions to occupy the same quantum state. Even so, ^{3}He also becomes superfluid at a temperature of around 1 mK. The superfluidity of ^{3}He arises from the pairing of fermionic ^{3}He atoms into bosonic Cooper pairs in a similar manner as electrons pair up in superconductors. The phenomenon was explained by Bardeen, Cooper, and Schrieffer in a microscopic description later to become known as the BCS theory [14]. Today, superfluid ^{3}He is probably the most sophisticated macroscopic quantum system, which we can investigate experimentally and claim to understand quantitatively. As such, it serves as an analog model for theories and phenomena elsewhere in physics, including not only condensed-matter physics but also particle physics and cosmology [15].

At temperatures below ~ 100 mK liquid ^{3}He behaves as a degenerate Fermi liquid as described by Landau [16]. An essential feature of Landau's theory is that the excited states above the ground state of a strongly interacting quantum system can be represented as a collection of weakly interacting quasiparticle excitations and all the thermal, transport, and response properties of the system are determined by the quasiparticle states which are close to the Fermi surface. According to the BCS theory, fermions, in the presence of attractive interaction, tend to form Cooper pairs in an energy shell of width $\sim k_B T_c$ around the Fermi energy e_F. The quantity T_c is the critical temperature below which these pairs are formed and k_B is the Boltzmann constant.

Remarkably, the Cooper pairing happens no matter how weak the attractive potential is. In superconductors, the attraction is due to the electron-phonon coupling, while in ^{3}He the pairing potential is provided by the weak Van der Waals interaction together with the spin-fluctuation exchange mechanism. The latter favors pairing with odd angular momentum l, which implies that the spin state must be a triplet due to the exchange symmetry of the Fermi statistics. The sim-

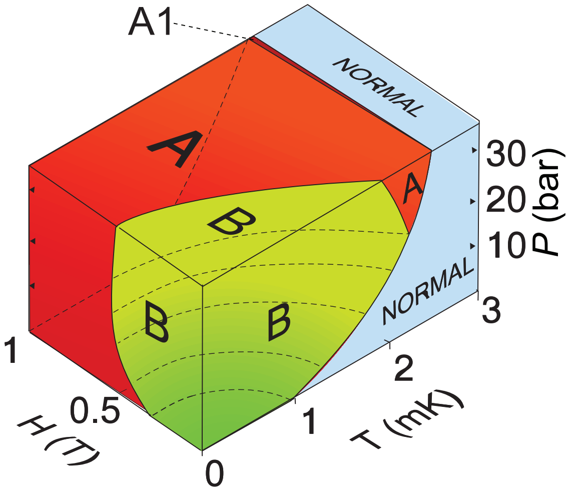

Fig. 1.1 Phase diagram of liquid ^{3}He. At atmospheric pressure ^{3}He liquifies at 3.2 K. At zero magnetic field the B phase occupies the largest part of the phase diagram below the pressure-dependent critical temperature T_c. The A phase, which in the absence of magnetic fields is stable only at high pressures and temperatures $T \geq 1.93$ mK, extends down to $T = 0$ if an external magnetic field $H \geq 0.34$ T is applied. The A1 phase exists only in a narrow temperature interval close to T_c, and only if $H > 0$.

ple spin-singlet s-wave pairing ($S = l = 0$), which is the pairing mechanism for conventional superconductors, is in any case prevented by the strong core repulsion. In superfluid ^{3}He, the Cooper pairs are formed in the spin-triplet orbital p-wave state, where the total spin and the angular momentum both equal one.

The pairing with $S = l = 1$ leads to an order parameter with 3×3 components. This enables the existence of various superfluid phases, three of which are stable in bulk ^{3}He. These are shown in the phase diagram in Fig. 1.1. At low pressures, in the absence of magnetic fields, the stable phase at all temperatures is ^{3}He-B, in which the Cooper pairs are formed in an admixture of all the three spin states. At high pressures another phase, ^{3}He-A, becomes more favorable due to the spin-fluctuation stabilization mechanism [17]. This phase is a so-called equal-spin-pairing state in which pairs form only in the $S_z = +1$ and $S_z = -1$ states. In a magnetic field, A phase can exist down to $T = 0$ and another state in a narrow temperature region at high pressures close to T_c, the A1 phase, becomes stable. The A1 phase contains only pairs with $S_z = +1$. Most of the experiments described in this thesis concern the B phase at temperatures $T < 0.4\,T_\mathrm{c}$.

The macroscopic wave function, or the order parameter in ^{3}He-B, is given by

$$A_{\mu j} = \mathbf{\Delta}_{\mu\nu} e^{i\varphi} \mathbf{R}_{\nu j}(\hat{\mathbf{n}}, \theta), \tag{1.1}$$

where $\mathbf{\Delta}$ is the temperature- and pressure-dependent superfluid energy gap and φ the common phase of the order parameter. The matrix $\mathbf{R}(\hat{\mathbf{n}}, \theta)$ describes the rotation of the spins with index μ relative to the orbital coordinates with index j around the unit vector $\hat{\mathbf{n}}$. In the energy minimum, the rotation angle equals $\theta = \arccos(-1/4)$ and is determined by the interaction between the nuclear dipole moments of the nuclei [6]. The so-called order-parameter texture is given by the spatial distribution of $\hat{\mathbf{n}}$. The equilibrium texture depends on many orientational effects including the interaction with the external magnetic field, surface effects at the boundaries of the ^{3}He sample, and the effect of rotation [18]. The length scale of the spatial variations is determined by the magnetic coherence length $\xi_{\rm H} \propto H^{-1}$. In ^{3}He-B in our experimental conditions $\xi_{\rm H} \sim 1$ mm.

Except at the lowest temperatures superfluid ^{3}He with density ρ can phenomenologically be described to consist of two interpenetrating components: a superfluid component with density $\rho_{\rm s}$ coexists with the normal component with density $\rho_{\rm n}$ such that $\rho = \rho_{\rm n} + \rho_{\rm s}$. The normal component has finite viscosity and carries all the entropy of the fluid. In the low-temperature limit, which is relevant to this thesis, the concept of this two-fluid model breaks down as the normal liquid becomes too dilute to allow viscous interaction. In this limit, the thermal properties of the system are determined by a dilute gas of ballistic elementary excitations with an effective mass m^* described by the Landau Fermi-liquid theory [19].

1.2 Quantized vortices and rotating superfluid

The superfluid velocity $\mathbf{v}_{\rm s}$ is proportional to the gradient of the phase factor $\nabla\varphi(\mathbf{r}, t)$. Therefore, superfluid flow is irrotational, i.e., $\nabla \times \mathbf{v}_{\rm s} = 0$. Rotation can be accommodated only by the creation of quantized vortices. Vortices are topologically stable string-like defects which cannot end in the bulk superfluid. As a consequence, they either form loops or terminate at a boundary. Vortices in superfluid ^{4}He have a singular core, where the order parameter vanishes.

Due to the multi-component order parameter of superfluid ^{3}He, many different vortex-core structures may exist [20]. At low temperatures in ^{3}He-B the vortex that is stable is a nonaxisymmetric vortex [21], where the order-parameter has a finite amplitude inside the hard core with the radius a comparable to the coherence length $\xi(T, P)$ of the order of 10 nm.

The superfluid flows around the vortex core with an azimuthal velocity $v_\phi = \hbar/(2m_3 r_v)$, where $\hbar = h/(2\pi)$ is the reduced Planck constant, $2m_3$ the mass of a Cooper pair consisting of two ^{3}He nuclei with the mass m_3, and r_v the distance from the center of the core. The flow is quantized with the circulation quantum $\kappa = h/2m_3 = 0.066\,\mathrm{mm}^2/\mathrm{s}$. The vortex lines are considered to be a part of the superfluid component but unlike the vortex-free superfluid, they interact with the normal fluid through a frictional interaction known as mutual friction [22, 23]. The mutual-friction force on vortex lines arises from the scattering of normal fluid excitations from the vortex cores. The velocity of a vortex-line segment is [24]

$$\mathbf{v}_\mathrm{L} = \mathbf{v}_\mathrm{s} + \alpha\hat{\mathbf{s}} \times (\mathbf{v}_\mathrm{n} - \mathbf{v}_\mathrm{s}) - \alpha'\hat{\mathbf{s}} \times [\hat{\mathbf{s}} \times (\mathbf{v}_\mathrm{n} - \mathbf{v}_\mathrm{s})], \tag{1.2}$$

where $\mathbf{v}_\mathrm{s}$ and $\mathbf{v}_\mathrm{n}$ are the local velocities of the superfluid and the normal components and $\hat{\mathbf{s}}$ a unit vector along the vortex line. The parameters α and α' are the pressure- and temperature-dependent mutual-friction parameters [25].

If a container with superfluid is brought into rotation at angular velocity Ω, the normal component corotates with the container in solid-body rotation with velocity $\mathbf{v}_\mathrm{n} = \mathbf{\Omega} \times \mathbf{r}$, where $|\mathbf{r}|$ is the radial distance from the rotation axis. As long as the sample remains free of vortices, the superfluid remains at rest. This state, which is analogous to the Meissner state in superconductors [26], is called the Landau state. At the so-called Feynman velocity $\Omega_\mathrm{c1} = \kappa/(2\pi R^2)\ln(R/a)$ it becomes energetically favorable to create the first vortex in a rotating cylindrical container with radius R. In practice, vortices are created at much higher angular velocities due to the energy barrier preventing vortex formation, and the real critical velocity depends on the roughness of the container surfaces (see Sec. 2.1).

The equilibrium state at constant rotation velocity Ω consists of a uniform array of rectilinear vortex lines parallel to the axis of rotation. The vortex density is determined by minimization of the free energy in the rotating frame and is given by the solid-body-rotation value $n_v = 2\Omega/\kappa$. The array is isolated from the container wall by a narrow annular vortex-free layer. The width of the vortex-free region $\sqrt{\kappa/(\sqrt{3}\Omega)}$ is only slightly larger than the intervortex distance [27].

1.3 Quantum turbulence

Turbulence is often defined as a complex and dynamic flow field, which involves processes spanning several orders of magnitude in spatial extent with aperiodic temporal dependence. In classical fluids, turbulence is ubiquitous and is of great importance in different fields ranging from aircraft engineering and meteorology to the evolution of galaxies.

The equation governing classical fluid dynamics is the Navier-Stokes equation

$$\frac{\partial \mathbf{v}}{\partial t} + (\mathbf{v} \cdot \nabla)\mathbf{v} = \frac{\mathbf{F}}{\rho} - \frac{\nabla P}{\rho} + \nu \nabla^2 \mathbf{v}, \tag{1.3}$$

where **F** is an external force per unit volume and ν the kinematic viscosity. The flow is often characterized by the ratio of the inertial term $(\mathbf{v} \cdot \nabla)\mathbf{v} \propto U^2/D$ and the viscous term $\nu \nabla^2 \mathbf{v} \propto \nu U/D^2$, where U and D are the characteristic velocity and the characteristic size of the system. This ratio $Re = UD/\nu$ is the so-called Reynolds number. When it is small, the dissipative forces dominate and the flow remains laminar. With increasing Re the strength of the flow disturbance which is required to trigger turbulence rapidly decreases [28].

Superfluid flow is inviscid, and the governing equation in the low-temperature limit where $\alpha' \ll 1$ is the coarse-grained hydrodynamical equation [29]

$$\frac{\partial \mathbf{v}_\mathrm{s}}{\partial t} + \nabla \mu_\mathrm{c} - (\mathbf{v}_\mathrm{s} \cdot \nabla)\mathbf{v}_\mathrm{s} = -\alpha \hat{\omega} \times ((\mathbf{v}_\mathrm{s} - \mathbf{v}_\mathrm{n}) \times (\nabla \times \mathbf{v}_\mathrm{s})), \tag{1.4}$$

where μ_c is the chemical potential and $\hat{\omega}$ a unit vector along the course-grained vorticity $\nabla \times \mathbf{v}_\mathrm{s}$. Equation (1.4) assumes that the vortices are locally polarized, and the contribution from the vortex-line tension is neglected. Here the relevant Reynolds number is the superfluid Reynolds number $Re_\alpha = (1 - \alpha')/\alpha \approx 1/\alpha$.

In the $T \to 0$ limit, the superfluid can be modeled as an inviscid and incompressible fluid, where turbulence involves vortex reconnections and tangle formation. In these conditions of quantum turbulence, numerical modeling and the interpretation of measurements become more manageable than in the case of classical viscous fluids. Different types of turbulent flows are characterized by the local density $L(\mathbf{r})$ of the vortices and their polarization. In its simplest form, turbulence in superfluids consists of a homogeneous and isotropic tangle of singly quantized vortex lines.

In the long-studied case of superfluid ^{4}He, turbulence can be detected, e.g., by ion trapping on vortex cores or second sound attenuation [24], while recent work on turbulence studies has been making use of transmission measurements of charged vortex rings [30] or trapping of micron-sized tracer particles in vortex tangles [31], as well as analyzing the drag force exerted on vibrating structures [32]. In superfluid ^{3}He, the traditional method to study vortex motion is nuclear magnetic resonance (see Sec. 2.3). At very low temperatures, in the limit $T/T_c \ll 1$, a powerful tool is the Andreev scattering of thermal excitations (see

Sec. 3.1). This technique has been developed and exploited at the University of Lancaster [33].

On length scales which are large compared with the intervortex distance $\ell = L^{-1/2}$ quantum turbulence often resembles its classical counterpart [34]. The energy is injected into eddies at length scales determined by the characteristic size of the flow disturbance. The large scale motion is achieved by partial polarization of vortices to bundles forming eddies of different sizes. As in classical turbulence, the energy cascades down with a Kolmogorov-type energy spectrum given by

$$E(k) = C\epsilon^{2/3}k^{5/3}, \tag{1.5}$$

where $C \approx 1.5$ is the Kolmogorov constant. Assuming the dissipation is determined by the length scale ℓ, the energy flux towards shorter length scales, i.e., inverse k, per unit mass is given by

$$\epsilon = \nu'\kappa^2 L^2, \tag{1.6}$$

where ν' is the effective kinematic viscosity. Using Eqs. (1.5) and (1.6) allows us to describe the late-time decay of vortex density [35] by

$$L = \frac{\sqrt{27C^3}D}{2\pi\sqrt{\nu'}\kappa}t^{-3/2}, \tag{1.7}$$

where the container size D determines the cutoff wavenumber $k_0 = 2\pi/D$. This type of turbulence, involving large-scale motion, is often called quasiclassical, whereas the lack of flow energy on scales larger than ℓ leads to ultraquantum turbulence [36, 37]. In the latter case, also known as Vinen turbulence, the line density is expected to decay as $L \propto t^{-1}$.

The value of ν' in Eq. (1.7) of quasiclassical decay depends both on temperature and the nature of the flow. Despite the fact that the derivation leading to Eq. (1.7) assumes homogeneous and isotropic turbulence, our experiments in paper **VIII** show that turbulence with high polarization of vortices can also decay as $t^{-3/2}$.

It is widely believed that as the energy flows to length scales smaller than the intervortex distance, it is transferred in a cascade of helical deformations of individual vortices called Kelvin waves [34]. There is an ongoing debate on the nature of the energy transfer from the classical Kolmogorov-like cascade to the Kelvin-wave cascade [38, 39, 40, 41]. At finite temperatures mutual friction provides dissipation at all length scales, and even at $T = 0$, the energy is ultimately dissipated when Kelvin waves at very large k induce phonon emission [42] in ^{4}He or quasiparticle emission [43] from vortex cores in ^{3}He-B.

Chapter 2

Experimental techniques

2.1 Rotating cryostat and experimental setup

The experiments described in this thesis were performed in a rotating refrigerator. The first version of the ROTA cryostat became operational in 1982, and since then, continuous improvements have been made to enhance its operation performance. Most of the experiments in this thesis required very low levels of residual heat leaks, which were obtained by installing a second rotating platform and making other smaller improvements, e.g., to the balance of the rotating cryostat and to the electrical isolation of the devices. In the current setup, ^{3}He-sample temperatures below 140 μK can be achieved with the help of multiple cooling stages. Comprehensive and detailed descriptions of the cryostat can be found in Refs. [44, 45, 46] and only a brief overview is given here.

The refrigerator floats on air bearings in order to achieve smooth rotation. Two tight-fit horizontal air bearings align the cryostat accurately along the rotation axis. Most of the equipment is placed above the cryostat on a separate carousel, which is only weakly mechanically coupled to the refrigerator. This carousel, driven by a separate motor, is synchronized to corotate with the lower parts. The electrical power is fed through a carbon-slip contacts and the means for data communication is provided by opto-coupled fiber connections along the axis on the top and at the bottom of the cryostat.

The cooling stages from the warmest to the coldest are a liquid helium bath, a ^{4}He-evaporation stage, a dilution refrigerator, and an adiabatic nuclear demagnetization stage [10]. During the rotation, the dilution fridge is disconnected from the external pumping system and operates in the so-called single-cycle mode, where the ^{3}He evaporated from the still is absorbed by an active charcoal cryopump.

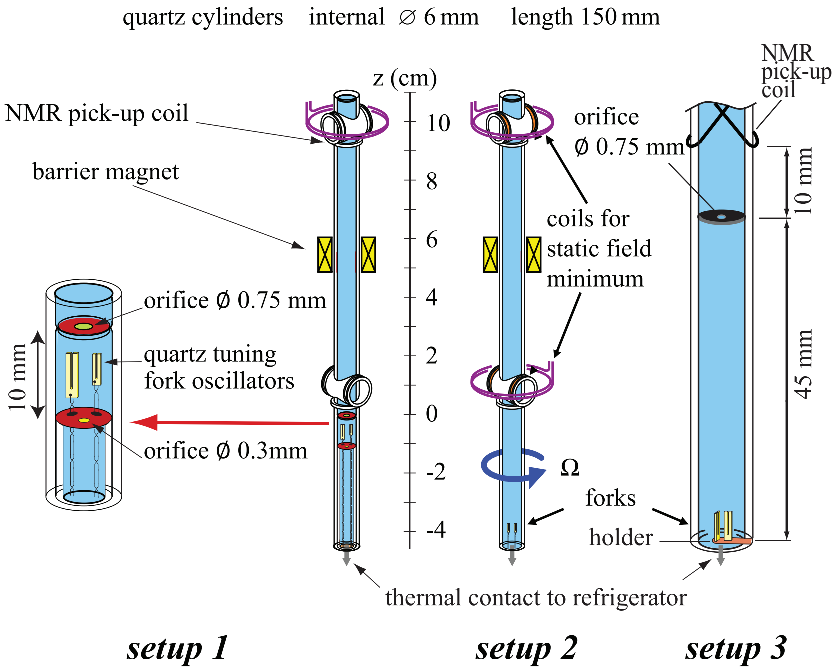
quartz cylinders internal ∅ 6 mm length 150 mm
z (cm)
NMR pick-up coil
barrier magnet
10
8
6
4
2
0
-2
-4
orifice Ø 0.75 mm
10 mm
quartz tuning fork oscillators
orifice Ø 0.3mm
orifice Ø 0.75 mm
coils for static field minimum
Ω
forks
holder
NMR pick-up coil
10 mm
45 mm
thermal contact to refrigerator
setup 1
setup 2
setup 3

Fig. 2.1 Experimental setups with the ^{3}He sample contained in a 15-cm-long quartz tube with 6 mm inner diameter. All setups contained NMR detection coils, quartz tuning forks, and a barrier magnet for A-phase stabilization. On the left *setup 1* with two division plates was optimized for calorimetric measurements and *setup 2* in the middle with no division plates for achieving the lowest possible temperatures, while *setup 3* on the right was a compromise between low temperatures and the possibility to maintain vortex-free rotation above the division plate with an orifice of 0.75 mm diameter. The minimum coils in *setup 1* and *setup 2* were used for creating a local minimum in the axially-oriented magnetic field **H**. In *setup 3* the pickup coils were wound directly on the quartz cylinder whereas in *setup 1* and *setup 2* coil holders were used.

The liquid ^{3}He is contained in a 15-cm-long fused quartz cylinder with the bottom end opening to a sintered-silver heat exchanger on to the nuclear stage. The sinter provides a good thermal contact with the nuclear cooling stage so that the superfluid ^{3}He at the bottom of the cylinder can be cooled down to below $0.14\,T_\mathrm{c}$.

Three different setups in Fig. 2.1, henceforth referred to as *setup 1*, *setup 2*, and *setup 3*, were used in the experiments described in this thesis. The inner diameter of the tubes was approximately 6 mm except for the 45-mm-long section of the bottom part of *setup 1*, where the inner diameter was 3.6 mm. The primary experimental tools available in all the setups were vibrating quartz tuning forks and external nuclear magnetic resonance (NMR) coils, which are described in Secs. 2.2 and 2.3 respectively. In *setup 1* and *setup 3* a 1-mm-thick division plate with a 0.75 mm orifice at the center located 45 mm from the bottom of the cylinder prevented vortices from the lower part of the tube to migrate to the upper volume. An additional division plate with a 0.3 mm pinhole was added in *setup 1* to increase the thermal impedance between the sample and the nuclear stage and thus, to enable calorimetric measurements with good sensitivity. In *setup 2* the goal was to minimize the sample temperature and thus, it contained no division plates. We used *setup 1* in papers **III**-**VIII**, *setup 2* in **VIII** and **IX**, and *setup 3* in **I**-**IV**. The barrier magnet between the two NMR coils made it possible to stabilize a layer of ^{3}He-A which separates the sample in two disconnected sections of B phase. This feature was utilized in papers **V** and **VI**.

Even though the Feynman critical angular velocity for vortex formation in a cylinder with a radius $R = 3$ mm is only $\Omega_{\rm c1} \sim 0.01$ rad/s, the energy barrier preventing the vortex formation enables vortex-free flow up to two orders of magnitude larger rotation velocities. The critical velocity $\Omega_{\rm c}$ for vortex formation in the cylindrical container depends largely on the roughness of the walls. To obtain as high $\Omega_{\rm c}$ as possible, the quartz container is carefully etched, cleaned, and evacuated from rest gases. Before each cooldown, the sample volume is flushed with pure ^{3}He gas and pumped carefully while heating the assembly to $50\,^\circ\mathrm{C}$. The critical velocities of the sample tubes used in our experiments varied in the range 1.7-2.0 rad/s and were found to slowly deteriorate from one cooldown to another, probably due to the accumulation of impurities on the cell walls.

2.2 Quartz tuning fork oscillators

Quartz tuning forks are commercially manufactured oscillators used for example as frequency control elements in digital watches. Owing to the piezoelectric nature of quartz, the mechanical excitation of the tuning fork can be replaced by electrical excitation. Provided that appropriate symmetry conditions of the crystal lattice are satisfied, a piezoelectric material is able to convert a voltage to a mechanical displacement. Conversely, a deformation in such a lattice generates electrical charges.

Figure 2.2 shows a photograph and a sketch of a quartz tuning fork with the prong length $\mathcal{L}$, thickness $\mathcal{T}$, and width $\mathcal{W}$. Forks are available in different sizes. A typical length is a few millimeters, while the thickness and the width are some

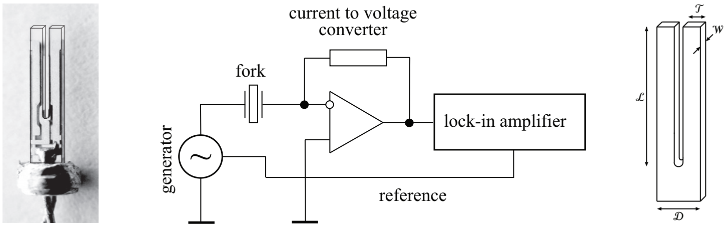

Fig. 2.2 Picture of a quartz tuning fork, the circuit diagram used for fork measurements, and a sketch of a fork. The fork is driven with a function generator with the excitation voltage U_0 in the range 10 µV-10mV depending on the damping caused by the surrounding medium. The piezo-electric current is amplified with a room-temperature I/V converter before being fed to a two-phase lock-in amplifier.

fractions of a millimeter. The two prongs of the fork oscillate in antiphase so that the center of mass remains at rest. The most typical resonance frequency is $f_0 \approx 32\,\mathrm{kHz}$. A major advantage in many applications is that no magnetic field is needed to drive the fork unlike the more conventional resonators used in cryogenic applications, such as vibrating wires [47]. Furthermore, forks are rather insensitive to magnetic fields when their magnetic leads are replaced with nonmagnetic ones [48].

Forks are highly sensitive to changes of the properties of the medium they are immersed in. They have become popular tools for studying quantum liquids since Clubb et al. [48] studied ^{3}He-^{4}He mixtures with them. We were the first to use forks to measure temperature, pressure, and viscosity in superfluids in paper **I**. Thereafter, they have been used to study quantum turbulence by us in paper **II** and by many others [49, 50, 51, 52, 53, 54] as well as classical turbulence in ^{4}He [55, 56].

Commercial forks are originally supplied in a closed metallic cylinder. To obtain the contact with the desired medium, the cylinder is removed or at least pierced. We also replace the original magnetic leads with superconducting wires.

The equation of motion for a quartz tuning fork, which can be modeled as a driven damped harmonic oscillator, is

$$\frac{\mathrm{d}^2x}{\mathrm{d}t^2} + \gamma\frac{\mathrm{d}x}{\mathrm{d}t} + \frac{K}{m}x = \frac{F}{m}, \tag{2.1}$$

where x is the displacement and m the effective mass of the resonator, γ the drag coefficient and K the spring constant. For a harmonic drive $F = F_0\cos(\omega t)$, the solution of Eq. (2.1) consists of the transient and steady state parts. The latter can be written as $x(t) = x_a\sin(\omega t) + x_d\cos(\omega t)$, where x_a and x_d are the absorption and the dispersion, respectively.

In our experiments, the fork is excited with an ac voltage $U = U_0\cos(\omega t)$. The piezoelectric effect makes the fork prongs to deflect from their equilibrium positions. The stresses due to these deflections induce charges and thus the current is proportional to the derivative of the fork deflection, that is

$$I(t) = a_\mathrm{f}\frac{\mathrm{d}x}{\mathrm{d}t}. \tag{2.2}$$

Here a_f is the fork constant, which can be determined experimentally [**I**]. The electrical model of a fork is an RLC series resonance circuit. The current response is measured either directly with a lock-in amplifier or with an I/V converter [57], the output of which is connected to a lock-in as shown in Fig. 2.2.

The dimensionless quantity, the so-called quality factor $Q = \omega_0/\gamma$, is widely used when discussing oscillators. At the resonance frequency ω_0 the mean absorbed power is at maximum. The full width of the resonance curve at half of the maximum power is $\Delta f = \gamma/(2\pi)$. If the driving force of the fork at resonance is stopped, it takes Q/π periods, i.e., $2/\Delta f$ s for the amplitude to decay to $1/e$ of the initial value [58]. The highest Q-values are obtained in vacuum at $T < 4$ K, where the linewidth $\Delta f_\mathrm{vac} \sim 10$ mHz of the forks we use is caused by intrinsic dissipation in the quartz crystal and by losses in the measuring circuit.

When the fork is immersed in liquid, f_0 decreases and Δf increases. The relations for the resonance frequency and the width as a function of fluid density ρ and viscosity η are [**I**]

$$\left(\frac{f_{0\mathrm{vac}}}{f_0}\right)^2 = 1 + \frac{\rho}{\rho_\mathrm{q}}\left(\beta + B\frac{\mathcal{S}}{\mathcal{V}}\sqrt{\frac{\eta}{\pi\rho f_0}}\right), \tag{2.3}$$

$$\Delta f = \Delta f_\mathrm{vac} + \frac{1}{2}\sqrt{\frac{\rho\eta f_0}{\pi}}\,\mathcal{C}\,\mathcal{S}\,\frac{(f_0/f_{0\mathrm{vac}})^2}{m_\mathrm{vac}}, \tag{2.4}$$

where ρ_q is the density of quartz, $\mathcal{V} = \mathcal{TWL}$, $\mathcal{S} = 2(\mathcal{T} + \mathcal{W})\mathcal{L}$, and $m_\mathrm{vac} = 0.24267\rho_q\mathcal{V}$ [**I**]. The fork parameters β, B and $\mathcal{C}$ can be determined experimentally from measurements in a fluid with known ρ and η. These parameters vary from fork to fork, which makes a calibration necessary.

Fig. 2.3 shows the temperature dependence of Δf in ^{4}He and ^{3}He both above and below the superfluid transition temperature. In normal ^{3}He, the viscosity,

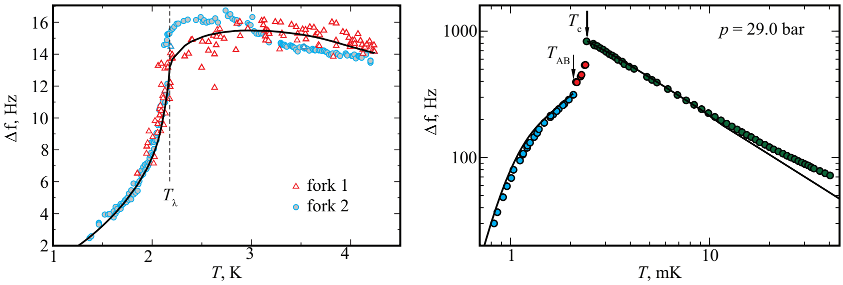

Fig. 2.3 Full width at half maximum of the absorbed power of quartz tuning forks in helium liquids. (*Left*) Widths of two quartz tuning forks in liquid ^{4}He at saturated vapor pressure. The solid line is a fit of the fork 1 data above the superfluid transition point T_λ to Eq. (2.4) using $\mathcal{C}$ as fitting parameter. The data on the physical properties of liquid ^{4}He are taken from Ref. [59]. (*Right*) Width of a fork in liquid ^{3}He at 29 bar pressure. The data are marked with circles. The width rapidly decreases below T_c and an abrupt discontinuity is seen at the AB transition. The solid line is the predicted behavior [60] of a vibrating wire resonator with the same density and the same vacuum resonance frequency as the fork. The wire diameter was fixed to 0.25 mm which is comparable to the dimensions of the cross section of the fork.

and thus the fork width, scales as T^{-2}. In both superfluids the linewidth rapidly decreases below T_c.

At the lowest temperatures in superfluid ^{3}He, the hydrodynamic description (2.3-2.4) is no more valid as the mean free path of excitations increases and the normal fluid penetration depth of rotational flow around the fork grows beyond all the relevant length scales [**I**]. This so-called ballistic regime in ^{3}He-B takes place below 0.3 T_c. As long as the prong velocity v_p is kept below the critical velocity where the resonator starts to break Cooper pairs [61], the dependence of the linewidth Δf on temperature is given by [62]

$$\Delta f = \Delta f_\mathrm{vac} + \zeta e^{-\Delta/k_B T}(1 - \lambda_f \frac{p_F}{k_B T} v_\mathrm{p}), \tag{2.5}$$

where p_F is the Fermi momentum and ζ and λ_f are geometry-dependent factors. At low pressures we use the so-called BCS weak-coupling value for the superfluid energy gap Δ in the $T \to 0$ limit [63] with the 0 bar value given by $\Delta(0)/k_B T_\mathrm{c} = 1.77$. Specific-heat measurements, for example by Greywall [64], show that the gap is linear in density. Todoschenko et al. performed a very accurate measurement of the superfluid gap at the melting curve [65]. At high pressures we use linear density interpolation between the weak-coupling gap and their value $\Delta_\mathrm{mc}/k_B T_\mathrm{c} = 1.99$ at the melting pressure.

The second term in the parenthesis in Eq. (2.5) with $\lambda_f \sim 1$ arises from the Andreev reflection (see Sec. 3.1) of thermal excitations from the potential flow field created by the fork prongs moving the liquid around them. When the fork is driven at low excitation, v_p is small and the velocity-dependent term in Eq. (2.5) can be neglected. Thus, calibrating the fork to act as a thermometer requires determining only the geometry-dependent factor ζ. At high pressures, the fork is calibrated at $T \sim 0.3\,T_\mathrm{c}$ against a ^{3}He-melting curve thermometer [66, 67], which is thermally coupled to the heat exchanger. We also use the longitudinal resonance frequency of the NMR response with known temperature dependence for calibration [68], especially at low pressures.

2.3 Nuclear-magnetic-resonance spectroscopy of ^{3}He

The traditional method to study superfluid ^{3}He is nuclear magnetic resonance. Since ^{3}He nuclei have a nonzero magnetic moment they can be excited to resonate in a magnetic field **H** at the so-called Larmor frequency $f_\mathrm{L} = \omega_\mathrm{L}/(2\pi) = |\gamma_\mathrm{He}|H/(2\pi)$, where $\gamma_{\mathrm{H}e} = -32.4 \cdot 10^6$ Hz/T is the gyromagnetic ratio of ^{3}He. For the basics of NMR we refer to [69] and for the theoretical basis of the NMR response in ^{3}He to [70].

We use the continuous-wave-NMR method where the frequency of the RF excitation field is kept constant and the strength H of the polarizing axial magnetic field is slowly varied. The square of the transverse NMR resonance frequency ω in ^{3}He-B is given by [70]

$$\omega^2 = \frac{1}{2}(\omega_\mathrm{L}^2 + \Omega_\mathrm{B}^2) + \sqrt{\frac{1}{4}(\omega_\mathrm{L}^2 + \Omega_\mathrm{B}^2)^2 - \omega_\mathrm{L}^2\Omega_\mathrm{B}^2 \cos\beta}, \tag{2.6}$$

where $\Omega_\mathrm{B}(p,T)$ is the longitudinal NMR resonance frequency [71] and β the angle between $\hat{\mathbf{n}}$ and **H**. In the limit $\Omega_\mathrm{B} \ll \omega_\mathrm{L}$ Eq. (2.6) can be written in the approximate form

$$\omega = \sqrt{\omega_\mathrm{L}^2 + \Omega_\mathrm{B}^2 \sin^2\beta} \approx \omega_\mathrm{L} + \frac{\Omega_\mathrm{B}^2}{2\omega_\mathrm{L}} \sin^2\beta. \tag{2.7}$$

Consequently, the frequency ω differs from the Larmor frequency only if $\hat{\mathbf{n}}$ is oriented along **H**, and the frequency shift $\omega - \omega_\mathrm{L}$ is always positive.

In the so-called local oscillator model, the sample is considered as a collection of noninteracting oscillators with the frequency $\omega(r)$ given by Eq. (2.6). The

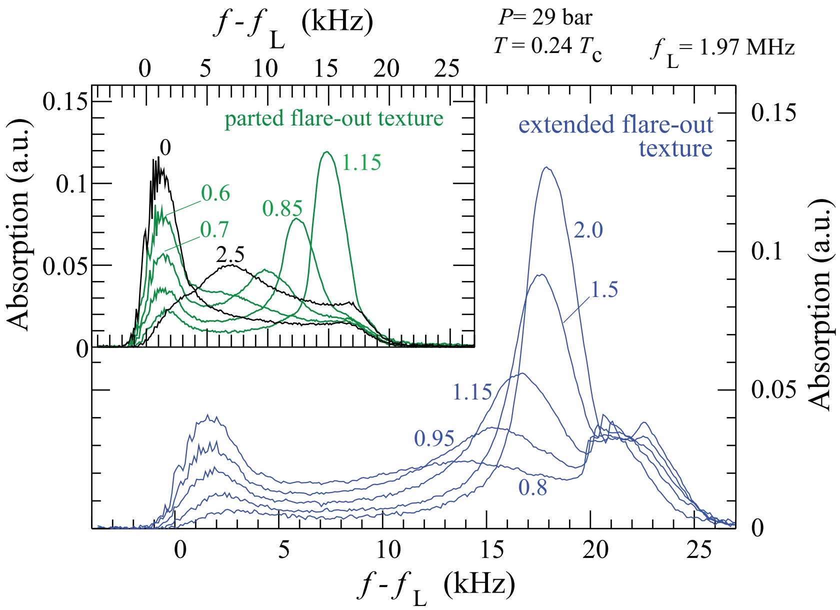

Fig. 2.4 NMR absorption spectra in vortex-free counterflow shown with blue and green lines and labeled by the corresponding rotation velocity in rad/s. For comparison, the black spectra marked as "0" and "2.5" represent the non-rotating state and the equilibrium vortex state at 2.5 rad/s, respectively. The main panel displays the high-velocity spectra above a textural transition at about 0.95 rad/s, while the low-velocity textures are shown in the insert [72]. The transition is of first order, as seen from the wide hysteretic overlap of the two textures from 0.8 to 1.15 rad/s.

total NMR response at given frequency ω is determined by summation over the individual contributions

$$f(\omega) = \frac{1}{V_\mathrm{s}} \int d^3\mathbf{r}\,\delta[\omega - \omega(\mathbf{r})], \tag{2.8}$$

where V_s is the volume of the sample in which the nuclear spins are excited.

In our measurements, the NMR detector coil is connected to a parallel capacitor to form an LC resonator. The inductance L_c of the coil changes with the dynamic susceptibility $\chi(\omega) = \chi_\mathrm{d}(\omega) - i\chi_\mathrm{a}(\omega)$, where $\chi_\mathrm{d}(\omega)$ and $\chi_\mathrm{a}(\omega)$ are the dispersion and absorption components. In practice the voltage across the inductance

$$L_\mathrm{c} = L_0(1 + \zeta_\mathrm{f}\chi(\omega)) \tag{2.9}$$

is compared to the voltage with the unloaded inductance L_0. The filling factor ζ_f is the fraction of the volume inside the coil filled by the ^{3}He sample. A detailed description of the measuring circuit can be found elsewhere [46].

At low rotation velocities, most of the NMR absorption occurs at frequencies close to the Larmor frequency since apart from the vicinity of the side walls β is small. With increasing counterflow $\mathbf{v}_\mathrm{n} - \mathbf{v}_\mathrm{s}$ in a cylindrical sample the NMR absorption starts to accumulate at $\sin^2\beta = 0.8$ giving rise to the so-called counterflow peak. As a function of the rotation velocity in the vortex-free state, the sample undergoes a series of textural transitions, whose behavior depends both on temperature and pressure [72]. Fig. 2.4 shows a set of NMR spectra in vortex-free counterflow measured with the lower spectrometer of *setup 1*. When the sample becomes filled with vortices, the counterflow peak disappears and most of the absorption is transferred back towards the Larmor value. The height of the counterflow peak is a sensitive probe of the vortex number especially at high temperatures $T > 0.5\,T_\mathrm{c}$, where single-vortex resolution can be achieved in the peak height [73].

Chapter 3

Experiments on superfluid dynamics in ^{3}He-B

3.1 Propagation of thermal excitations in the presence of vortices

In the ballistic regime of excitation transport, thermal equilibrium is obtained via interaction between the thermal excitations and the diffusively scattering container walls, while the collisions between the excitations can be neglected. Superfluid flow fields, however, can constrain their trajectories.

In the rest frame of the superfluid, the dispersion relation $E(\mathbf{p})$ of excitations is symmetrical with the minimum energy Δ. The standard picture of Andreev reflection considers an excitation moving towards a changing energy gap [74]. In ^{3}He-B, the superfluid flow field modulates the minimum in the excitation spectrum. Using the notation of Barenghi et al. [75], the energy E of the excitation with momentum $\mathbf{p}$ in the flow field around a vortex is given by

$$E(\mathbf{p}) = \sqrt{\epsilon_p^2 + \Delta^2} + \mathbf{p} \cdot \mathbf{v_s}, \tag{3.1}$$

where $\epsilon_p = p^2/2m^* - \epsilon_F$ is the effective kinetic energy of the excitation measured with respect to the Fermi energy ϵ_F and $p = |\mathbf{p}|$. Excitations with $\epsilon_p > 0$ are called quasiparticles and excitations with $\epsilon_p < 0$ are called quasiholes. For quasiparticles the group velocity $\mathbf{v}_\mathrm{g}(E) = dE/d\mathbf{p}$ is parallel to the momentum $\mathbf{p}$ whereas for quasiholes it is antiparallel. The ratio m^*/m_3 varies from about 3 at zero pressure to about 6 at the melting pressure [76].

The consequence of the interaction term $\mathbf{p} \cdot \mathbf{v}_\mathrm{s}$ is that an excitation traveling with insufficient energy to overcome the potential energy barrier created by the superfluid flow field has no forward-propagating states due to the superflow gradient $\nabla\mathbf{v}_\mathrm{s}$ along the flight path. When the excitation reaches the minimum of the spectrum, it retraces its trajectory as an excitation on the other side of the minimum as its group velocity changes sign. In other words, a quasiparticle Andreev reflects as a quasihole and vice versa with a very small momentum transfer. At the lowest temperatures, the Andreev scattering from the superfluid backflow around an oscillating object dominates the damping force on the object [77]. A more detailed description of the Andreev-reflection process in ^{3}He-B can be found, e.g., in Refs. [33] and [53] and the references therein.

Since the excitation trajectories are also modified by the superflow associated with quantized vortices, the Andreev reflection provides a tool to study different vortex structures even at ultralow temperatures, where practically all other methods become insensitive. The cross section of Andreev reflection is substantial even for low vortex densities providing a sensitive probe of the superfluid flow field [75, 78]. In practice, the presence of vortices can be inferred from the variations in thermal damping of vibrating objects, such as vibrating wires [79, 80, 81, 82] or quartz tuning forks, as in our measurements in papers **II**, **VII**, and **VIII**.

3.1.1 Andreev scattering from a turbulent vortex tangle

In our experiment described in paper **II**, Andreev reflection of thermal excitations measured with quartz tuning forks was utilized to study quantum turbulence at temperatures below $0.25T_\mathrm{c}$. One, the so-called generator fork, was used for producing a turbulent vortex tangle, and another, the so-called detector fork, for detecting it.

In the experiment done in *setup 3* the damping due to thermal excitations was measured with the detector fork, driven at low velocity, while the generator fork was driven at a velocity exceeding the pair-breaking velocity. As in similar measurements with vibrating wires [83], the result was counterintuitive: the damping of the detector due to thermal excitations decreased despite the fact that the total number of excitations in the system increased. The reason is that the turbulent vortex tangle created by the generator diminished the heat flux reaching the detector by creating an Andreev-reflecting shadow for thermal excitations emanating from the container walls. This effect is demonstrated in the left panel of Fig. 3.1, where square pulses are fed to the generator at relatively high velocity.

The right panel in Fig. 3.1 shows how the fractional change in the detector damping behaves as a function of the generator velocity. Here the direct contribution from the heat flow produced by the generator is subtracted. The resulting dependence resembles that measured with vibrating wires [83]: With increasing generator velocity more vortices are produced, the line density in the tangle increases and its spatial extent grows. Both effects increase the screening of the detector and help to extend the cooling to higher generator drives. Qualitatively this result was found to be independent of which fork is used as generator and which as detector. However, using fork 1 in the inset of Fig. 3.1 as a generator produced a somewhat larger screening effect. Since the vortices are probably created mostly at the direction of oscillation, the turbulence created both above and below fork 1 in Fig. 3.1 shadow the quasiparticle flux incident on fork 2. The turbulence from fork 2, however, is created on the left and right of the fork. The vortices on the right barely contribute to the screening, since the same space angle from the center of fork 1 is already covered by the turbulence on the left from fork 2. Consequently, the turbulence created by fork 1 screens a larger fraction of the incident quasiparticle flux on fork 2 than in the opposite case.

In later papers [53, 62] similar features were observed and attributed to lower fork velocities. This discrepancy, which does not affect the qualitative result, could originate from a possibly erroneous velocity calibration used in the measurements in *setup 3*. In later measurements in *setup 1* and *setup 2*, a more reliable method of the power and velocity calibration was used. In any case, the critical velocity of the generator at which the reduction in the damping started was much lower than what has been measured with wires [83]. A plausible reason is that due to the rectangular shape of the fork, the critical velocity for vortex formation was reached locally at the sharp edges already at very low prong velocity.

3.1.2 Quasiparticle scattering from a cluster of vortices

Before our studies in paper **VII** the Andreev-scattering techniques had only been used to detect turbulent vortex tangles, which for interpretation were assumed to be homogeneous and isotropic, but which in practice were of unknown density and poorly known spatial extent. Thus, it had not been possible to compare theoretical predictions of heat transport in vortex systems directly to experimental results. In paper **VII**, we provided such a comparison and justified the use of the Andreev reflection technique as a visualization method of vortices in superfluid ^{3}He-B in the limit of vanishing normal fluid density.

In the experiment, we studied the heat transport by excitations through an array of rectilinear vortices in the steady state of rotation. The experiments were performed in *setup 1*. The upper part of the cylindrical container acted as a bolometer, an enclosure with a weak thermal link to the outside superfluid via the small orifice in the lower division plate [84]. The volume was furnished with

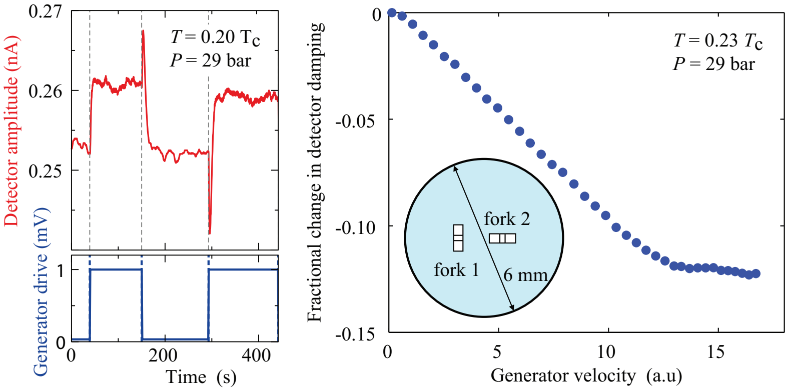

Fig. 3.1 Generation and detection of turbulence in ^{3}He-B using two quartz tuning forks. One fork, acting as a generator is driven at different steady drive levels to generate a turbulent tangle. The presence of the tangle is observed as a decrease in the damping of another fork, the detector. (*Left*) Original time trace of the amplitude of the detector fork at resonance, which is inversely proportional to the damping, as the drive of the generator fork is switched on and off. (*Right*) The relative change of the resonance width of the detector versus the oscillation amplitude of the generator, after subtracting for the temperature rise owing to the heat produced by the generator fork. (*Inset*) Top view of the mounting of the two forks in the sample cylinder.

two quartz tuning fork resonators, one acting as a thermometer and the other as a heater. The heater was used for generating a beam of ballistic excitations through the orifice. The nuclear refrigerant was demagnetized to very low temperatures so that the volume below the bolometer was below $0.15 T_c$, whereas the bolometer remained at $0.20\, T_c$. The large difference in the excitation densities allowed us to neglect the flow of background thermal excitations from the lower volume to the bolometer in our analysis.

All the power entering the bolometer must leave through the hole at the bottom as a flux of energy-carrying excitations. Assuming thermal equilibrium inside the bolometer the power is given by

$$\dot{Q}(\Omega) = \int N(E) v_g(E) E f(E) \mathcal{T} dE dx dy d\phi d\theta, \qquad (3.2)$$

where $N(E)$, $v_g(E)$ and $f(E)$ are the quasiparticle density of states, their group velocity, and the Fermi distribution function, respectively. In the limit $k_B T \ll \Delta$ the latter reduces to the Boltzmann distribution $f(E) = e^{-E/k_B T}$. The transmis-

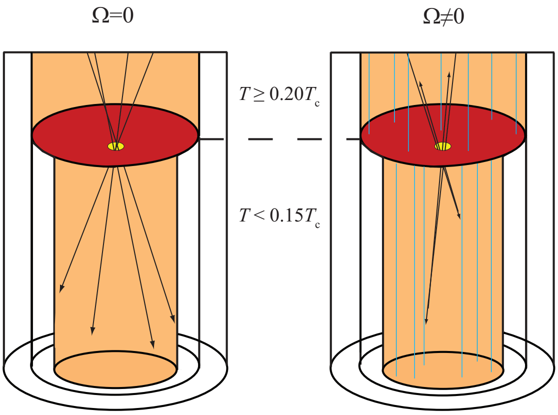

Fig. 3.2 Sketch of the experiment on the propagation of excitations in an array of vortices. In the system at rest ($\Omega = 0$), all the excitations which do not migrate back to the bolometer due to diffuse scattering from the walls are thermalized in the heat exchanger at the bottom. In rotation ($\Omega \neq 0$), part of the beam is Andreev reflected from the cluster of vortices below the orifice.

sion function $\mathcal{T} = \mathcal{T}(E, x, y, \phi, \theta, \Omega)$ is equal to one if an excitation leaving the bolometer (at position (x, y) on top of the orifice to direction (ϕ, θ)) reaches the heat exchanger and zero if it is reflected back. The integration goes over the cross section of the orifice, $\phi \in (0, 2\pi)$, $\theta \in (0, \pi/2)$ and $E \in (\Delta, \infty)$. The power $\dot{Q}_{\text{gen}}$ generated inside the radiator can now be expressed as the sum of the Ω-dependent residual heat leak $\dot{Q}_{hl}$ to the bolometer and the direct power P_{gen} from the excitations produced by the heater fork

$$\dot{Q}_{\text{gen}} = \dot{Q}_{hl}(\Omega) + P_{\text{gen}} = \frac{4\pi k_B p_F^2}{h^3} T e^{-\frac{\Delta}{k_B T}} (\Delta + k_B T) A_h(\Omega). \tag{3.3}$$

Here $A_h(\Omega)$ is the effective area of the orifice, which is reduced when part of the excitations is scattered back to the bolometer.

In the measurement, the heater fork was driven to create the desired excitation beam corresponding to the power P_{gen} leaving the bolometer. By controlling the rotation velocity, and thus the vortex density, we could control the fraction of Andreev reflected excitations. As illustrated in Fig. 3.2, the flow field created by the vortices reflected part of the beam back to the radiator by Andreev scattering. As a consequence, the temperature increase above the orifice was larger than with the same applied heating in the absence of vortices. The fraction Γ of heat reflected back into the radiator, which we call the reflection coefficient, can be

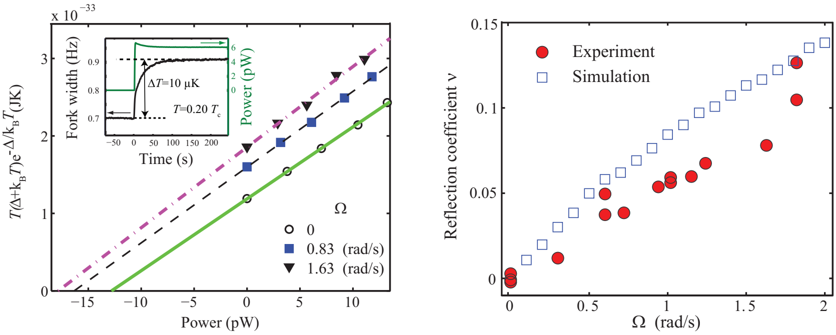

Fig. 3.3 (*Left*) Temperature-dependent part of the power leaving the bolometer as a function of heating power at three different rotation velocities at 29 bar pressure. The temperature is obtained from the linewidth of the detector fork. The data points are averages from data measured for about 10 minutes at each power. The intercept of the linear fit with the power axis gives the residual heat leak to the sample, while the effective area is given by the inverse of the slope. The slope, the heat leak, and the scatter in the data all increase with increasing angular velocity. The inset shows an example of the detector response to a heating pulse starting at time $t = 0$ for $\Omega = 0$. (*Right*) The fraction Γ of the heat Andreev reflected back into the bolometer radiator, as obtained from our steady-state measurements. The temperature inside the radiator is $0.20\ T_\mathrm{c}$. The simulation points are obtained by integrating Eq. (3.2) numerically and solving equations (3.3) and (3.4) for Γ.

obtained from Eq. (3.3) as

$$\Gamma(\Omega) = 1 - \frac{A_h(\Omega)}{A_h(0)}. \tag{3.4}$$

At each rotation velocity, we applied different power inputs to the radiator and measured the corresponding equilibrium temperature with the thermometer fork. Plotting all the temperature-dependent parts in Eq. (3.3) as a function of the power P_gen yielded a straight line (left panel of Fig. 3.3). The effective area A_h could be obtained from the inverse slope of the line and the heat leak $\dot{Q}_{hl}$ from the intercept with the power axis.

The right panel of Fig. 3.3 shows the reflection coefficient as a function of the rotation velocity. In the measured rotation velocity range, the dependence of Γ on the vortex density was found to be approximately linear. We believe that the main source of scatter in the experimental data came from the variation of the power calibration of the heater fork.

In our numerical simulations, the transmission function $\mathcal{T}$ was calculated for our geometry at different rotation velocities, and the integral in Eq. (3.2) was solved numerically using Monte Carlo integration with importance sampling. For solving $\mathcal{T}$, we traced whether the excitations leaving the bolometer with properly distributed energies, directions, and positions above the orifice, were reflected back or not. Setting the right hand side of Eq. (3.3) to equal that of Eq. (3.2) for $\Omega = 0$ (no vortices) and $\Omega \neq 0$ (with vortices) we obtained $A_h(0)$ and $A_h(\Omega)$, which allowed us to solve the reflection coefficient from Eq. (3.4). The simulations used the exact geometry of our experimental setup including the thickness and the shape of the radiator orifice. Instead of solving for the full equations of motions for excitations, which would have required too much computing power, only the vortices for which the impact parameter of the excitation was small enough to allow Andreev reflection were considered. We did not assume perfect retro-reflection but took into account the small Andreev reflection angle $\Delta\varphi = \hbar p_F^{-1}\sqrt{\pi/(3\xi b)}$ [75]. The wall scattering was assumed to be diffuse.[1] The reflection coefficient as a function of the rotation velocity from the numerical simulations (open square symbols) in the right panel of Fig. 3.3 is in a good agreement with the measurements (red bullets) thus supporting the current understanding of Andreev reflection.

3.2 Laminar and turbulent flow responses to a change of rotation

Fluid motion can be generated by changing the angular velocity Ω of the rotating container. Typically, a step change from some Ω to 0 or from 0 to Ω is applied for simplicity. The response of the superfluid to the former is called the spin-down and the latter the spin-up of the superfluid. In classical fluids, the response of the fluid in such experiments is governed by the frictional forces at boundaries and becomes unstable at relatively low Reynolds numbers [85]. Also in superfluid ^{4}He, where vortex pinning at the container walls plays a significant role due to the small vortex core radius, a rapid change of the container angular velocity is generally expected to generate turbulence [30].

In superfluid ^{3}He the situation is different, since in the case of smooth walls, the coupling to the container is accomplished mainly by friction in bulk volume. Due to the at least two orders of magnitude larger vortex core radius in ^{3}He-B compared to superfluid ^{4}He, surface pinning and surface friction do not substantially influence the dynamics as long as the container walls are relatively smooth.

---

[1] The validity of the assumption is discussed in Sec. IV of paper **VII**.

Therefore, the superfluid does not couple to the boundaries directly, but instead, through volume forces to the normal fluid, which is stationary in the reference frame of the container.

At high temperatures and large mutual friction, vortex motion is laminar, but as the mutual-friction coupling vanishes exponentially in the zero-temperature limit, the flow of vortices is easily destabilized and is expected to become turbulent. However, our noninvasive NMR measurements in ^{3}He-B, which are presented in papers **III** and **IV**, show that in an axially symmetric environment the spin-down and spin-up flows are laminar up to $Re_\alpha \sim 10^3$.

The laminar response in a cylindrical container rotating at an angular velocity Ω corresponds to a special case of the course-grained hydrodynamical equation (1.4), where the superflow is solid-body-like with angular velocity $\Omega_s = (\nabla \times \mathbf{v}_\mathrm{s})/2$. This requires that vortices remain highly polarized along the axis of the cylinder and thus, vortex reconnections play no role. In this case, taking a curl of both sides simplifies Eq. (1.4) to

$$\frac{d\Omega_s(t)}{dt} = 2\alpha\Omega(t)[\Omega(t) - \Omega_s(t)]. \tag{3.5}$$

For a step change of the rotation drive at $t = 0$ from an angular velocity Ω_0 to rest the solution of Eq. (3.5) is given by

$$\Omega_s(t) = \frac{\Omega_0}{1 + t/\tau}, \tag{3.6}$$

where $\tau = (2\alpha\Omega_0)^{-1}$. In real experiments, the change of rotation velocity is done at finite rate, in our case typically at $a = d\Omega/dt = -0.03$ rad/s^2. During the deceleration, i.e., for $-\Omega_0/a < t < 0$, the solution of Eq. (3.5) is

$$\Omega_s(t) = \frac{\sqrt{a}e^{\alpha(t+\Omega_0/a)(\Omega_0 - at)}}{\tau_0\sqrt{a} + \sqrt{\pi\alpha}e^{\alpha\Omega_0^2/a}\mathrm{erf}(\sqrt{\alpha a}t)}, \tag{3.7}$$

where $\tau_0 = \Omega_0^{-1} + \sqrt{\alpha/a}\exp(\alpha\Omega_0^2/a)\mathrm{erf}(\sqrt{\alpha/a}\Omega_0)$. At low temperatures, where $\alpha \ll a/\Omega_0^2$ the superfluid velocity at the end of the deceleration is very close to Ω_0 and consequently, Eq. (3.6) can be used at all times $t > 0$.

In paper **VI** we demonstrated how the increased surface friction on the interface of the A and B phases of superfluid ^{3}He makes the spin-down response turbulent. In paper **VIII** we showed that deviations from ideal cylindrical symmetry in the flow environment and a presence of a rough surface, which enhances vortex pinning, cause the early decay to support turbulent flow.

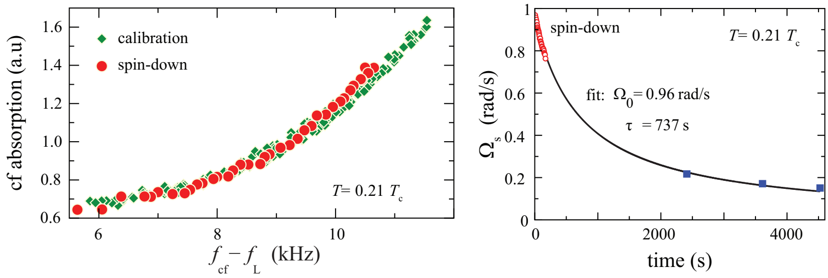

Fig. 3.4 (*Left*) Calibration of the counterflow peak for vortex-density measurements. The height of the counterflow peak in the steady state of vortex-free rotation (green diamonds) is shown as a function of the frequency shift $f_{\mathrm{cf}} - f_{\mathrm{L}}$ together with corresponding record in spin-down measurements (red circles). (*Right*) Spin-down response. Using the calibration in the left panel, the superfluid angular velocity $\Omega_s(t)$ is plotted as a function of time during spin-down after reaching $\Omega = 0$ at $t = 0$. The response can be fitted to Eq. (3.6), yielding the characteristic spin-down time $\tau = 737\,\mathrm{s}$ and Ω_0 corresponding to solid-body rotation at 0.96 rad/s, which was left after a deceleration from 1.0 rad/s to zero at $\dot{\Omega} = -0.03\,\mathrm{rad/s}^2$. The red circles are obtained directly by tracking the counterflow peak height whereas the blue squares are extrapolated from the subsequent spin-ups.

3.2.1 Dissipation of laminar vortex flow

At temperatures above $0.2\,T_{\mathrm{c}}$ both the height and the shift from the Larmor frequency f_L of the counterflow peak in the NMR absorption spectrum remain sensitive to changes in the amount of global counterflow. Thus, after determining their Ω-dependence in the state of vortex-free counterflow, they can be used to identify the vortex state during dynamic processes involving changes in vortex density. In the case of laminar solid-body-like flow at constant temperature there is a 1-to-1 correspondence both between the counterflow-peak amplitude I_{cf} and its frequency shift $f_{\mathrm{cf}} - f_{\mathrm{L}}$, and between the superfluid angular velocity Ω_s and $f_{\mathrm{cf}} - f_{\mathrm{L}}$.

The left panel of Fig. 3.4 shows an example of the counterflow-peak height as a function of its frequency shift measured in vortex-free rotation. If after a change of rotation velocity I_{cf} as a function of $f_{\mathrm{cf}} - f_{\mathrm{L}}$ corresponds to the calibration measurement, we can conclude that the superflow in the bulk volume is laminar, as in the case of the spin-down response shown by the red circles in the left panel of Fig. 3.4. Deviations from this correspondence would indicate depolarization of the vortices from their axial orientation.

Our spin-down and spin-up measurements in the upper volume of *setup 1* showed

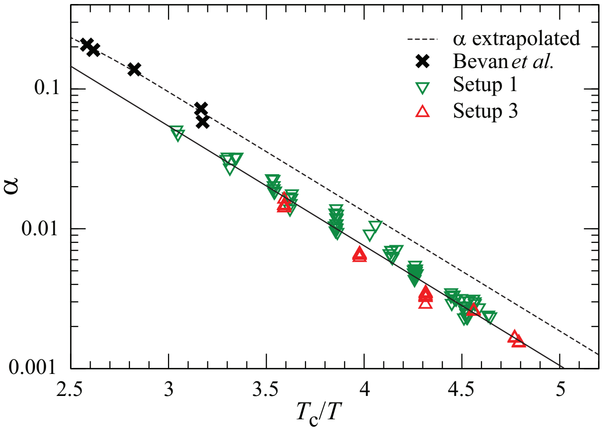

Fig. 3.5 The mutual-friction parameter $\alpha = (2\tau\,\Omega_0)^{-1}$ on the vertical scale versus normalized inverse temperature T_c/T. The solid line shows the fitted value $\alpha = 21\,\exp(-1.968\,T_\mathrm{c}/T)$. The measurements of τ (open triangles) are compared to the extrapolation (dashed line) for $\alpha(T)$ measured above $0.35\,T_\mathrm{c}$ in Ref. [86] (×).

that in a cylindrically symmetric environment both the spin-down and the spin-up responses remain laminar down to $0.20\,T_\mathrm{c}$. In the experiments, a step change of rotation to rest at $t = 0$ was applied and the corresponding decay of counterflow was translated into the superfluid angular velocity Ω_s. The right panel of Fig. 3.4 illustrates that the laminar solution (3.6) with $\Omega_0 = \Omega(t = 0)$ agrees well with the experiment. At $0.20\,T_\mathrm{c}$, the counterflow peak disappears completely when the angular counterflow velocity $|\Omega_s - \Omega|$ drops below 0.75 rad/s (red circles). After that had happened more points could be collected by increasing the rotation velocity rapidly back to some large value, where the counterflow becomes visible again, following the counterflow-peak height and its frequency shift, and subsequently extrapolating back to the moment when the velocity was changed (blue squares).

The laminar nature of the flow was also confirmed by numerical simulations by R. Hänninen using the vortex-filament method. A large deviation from the cylindrically symmetric geometry was needed to turn the response turbulent in the simulations. Turbulent response was obtained in a cubic container or in a tilted cylinder with the tilt angle higher than 30° (see Fig.2 in paper **III**).

The measured characteristic time constant $\tau = (2\alpha\Omega)^{-1}$ allowed determining the mutual-friction parameter $\alpha(T)$ down to much lower temperatures than be-

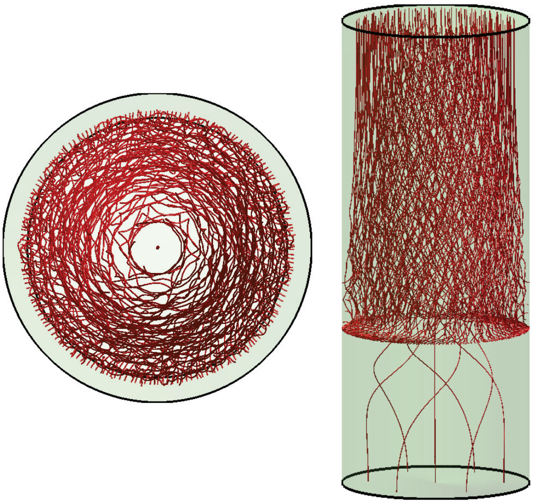

Fig. 3.6 Vortex configuration from vortex-filament calculations during spin-down of the superfluid component 30 s after a step-like reduction of Ω from 0.25 rad/s to zero. (*Left*) Top view into the cylinder showing a hollow region in the center and twisted vortices around it. (*Right*) Side view showing the A-phase section on the bottom with only a few vortices left, while in the B-phase the AB interface at large r is covered with vortices bending to the cylindrical wall. Above the interface the vortices are helically twisted around the central axis. Their polarization parallel to the axis increases with distance from the interface.

fore. In Fig. 3.5 $\alpha(T)$ obtained from the NMR measurements of spin-down is plotted together with earlier data of Bevan et al. [86, 87]. Given the uncertainties in the temperature calibration in Refs. [86, 87] and paper **III**, agreement can be considered excellent. Our results also prove that the scaling of the superfluid energy gap Δ suggested in Refs. [86, 87] is incorrect.

3.2.2 Spin-down response at the AB interface

By applying a magnetic field to a localized region of the superfluid, a two-phase sample, where a slab of ^{3}He-A coexists with ^{3}He-B, can be created. In our experiments, a barrier magnet, a small superconducting solenoid around the cylinder, provided an axially-oriented magnetic field for stabilizing an A-phase layer located 6 cm away from the top of the cylindrical container. In *setup 1* (Fig. 2.1), this divided the topmost volume into two identical B-phase sections.

The vortex dynamics in the two phases is very different. One reason is the significantly larger mutual friction in the A phase at low temperatures [87]. In the measurements reported in paper **VI** we examined the responses of the B-phase vortices to a step change in the rotation velocity Ω at the temperature $0.20\,T_{\mathrm{c}}$. The presence of A phase was found to make the dynamics faster indicating enhanced turbulence-induced dissipation.

As in the measurement described in Sec. 3.2.1, the height and the frequency shift of the counterflow peak were followed during the spin-down of the superfluid with and without the A-phase layer in the middle of the sample. In the presence of the A-phase slab the response turned out to be significantly faster, and the peak height versus frequency trajectory did not follow that corresponding to a uniform array of vortices. Instead, the frequency shift was larger at given amplitude of the counterflow peak.

The results were explained by the additional force exerted on the B-phase vortex ends at the AB interface. Due to the large mutual friction α_{A}, the vortices in the A-phase spiraled rapidly in a laminar fashion to the wall of the container. Consequently, the vortex density in the center of the cylinder initially reduced faster than at larger radii. This behavior was demonstrated by vortex filament calculations done by R. Hänninen. A snapshot of such a calculation is shown in Fig. 3.6.

The observations from both the experimental and the numerical data suggested a simple model to analyze the vortex distribution during the spin-down. In the model, we assumed that all the vortices were compressed into an outer cylindrical shell with the uniform initial density $n_0 = 2\Omega_0/\kappa$ while the center remained free of vortices. During the spin-down the radius r_{s} of the empty region was assumed to grow gradually until all the vortices were annihilated. The NMR spectra calculated with texture-calculation procedure [89] for this crude shell model agreed surprisingly well with the measured peak height versus frequency trajectory, as demonstrated in the left panel of Fig. 3.7. This allowed us to fit the observed counterflow-peak amplitude and its position to the shell model using r_{s} as an adjustable parameter.

The right panel of Fig. 3.7 shows the spin-down response of the normalized superfluid angular velocity with and without the A-phase. The former was obtained from the fitted radius r_{s} as $\Omega_s/\Omega_0 = 1 - (r_{\mathrm{s}}/R)^2$ and the latter from comparison to direct calibration measurements as described in Sec. 3.2. Again, after disappearance of the counterflow peak, more points could be collected by extrapolating the subsequent spin-ups.

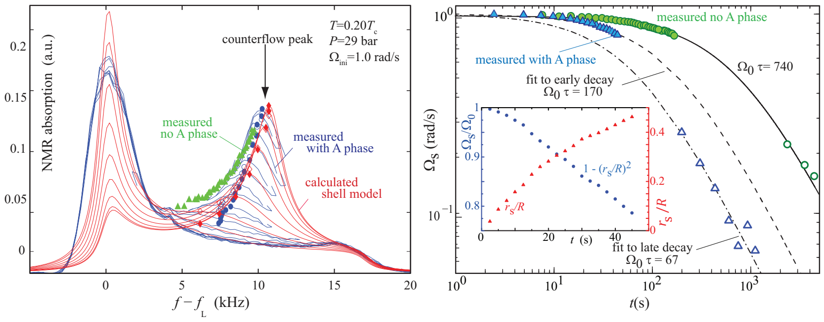

Fig. 3.7 (*Left*) NMR spectra during spin-down. The line shapes for the two-phase sample (red curves) have been calculated using the cylindrical shell model. The decreasing counterflow peak heights (red lozenges) correspond to increasing radius r_s of the central vortex-free cylinder in 20 µm steps, starting from $r_\mathrm{s} = 0$. The blue curves are from the measurements where the counterflow peak is monitored continuously by sweeping around its maximum (blue dots) during its decay. The green triangles show the measured peak trajectory in laminar spin-down in the absence of the A-phase layer [88]. (*Right*) Superfluid angular velocity Ω_s during spin-down. The response of the two-phase sample (blue triangles), analyzed as shown in the inset, is compared to that measured without the A-phase slab (green circles). The filled symbols correspond to the counterflow peaks measured during the spin-downs, while the open symbols represent extrapolations from the subsequent spin-ups (see text). The fitted curves represent $\Omega_\mathrm{s}(t) = \Omega_0/(1+t/\tau)$. *(Inset)* Cylindrical shell model of the two-phase sample, fitted to the measured spin-down as a function of time t. *(right vertical axis)* Normalized radius r_s/R (red triangles) of the vortex-free central cylinder, and *(left vertical axis)* equivalent normalized solid-body vortex density $\Omega_\mathrm{s}/\Omega_0 = 1-(r_\mathrm{s}/R)^2$ (blue dots).

With the A-phase slab, the response was found to be faster and not of the laminar form with one time constant τ as in Eq. (3.6). This feature, which was backed up by vortex-filament calculations in paper **VI**, indicated reconnection-driven turbulent dissipation. The weakly turbulent response in the presence of the AB interface, as opposed to the laminar response in the absence of it illustrates the importance of the surface friction at the vortex ends to the motion of vortices. Since the response in the absence of the A phase was found to be laminar, the surface friction on the walls of the cylinder wall must have been weak and no substantial amount of vortices could have been pinned on isolated surface defects on the container wall.

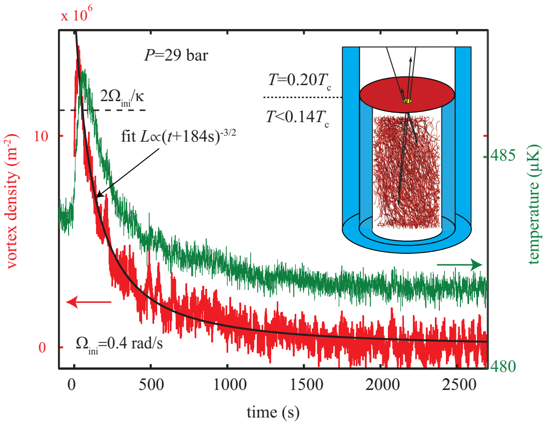

Fig. 3.8 Temperature T in the bolometer and an estimate for the lower limit of the vortex density L, after bringing the container to rest from Ω_{ini}=0.5 rad/s at $t = 0$. The vortex density is inferred from the fraction of Andreev-reflected thermal excitations, as discussed in the text. The solid line is a fit to $L \propto (t+\tau)^{-3/2}$ dependence after the initial overshoot in the data. (*Inset*) The principle of the measurement: The vortices below the orifice reflect some fraction of the thermal excitations back to the bolometer. The fraction Γ depends on the density and configuration of these vortices at the lower temperature $T < 0.14T_{\text{c}}$.

3.2.3 Quasiparticle-scattering measurements of vortex flow created in a spin-down to rest

A change from a laminar to a turbulent spin-down response can be brought about by deviations in the flow geometry from axial symmetry or, as demonstrated in Sec. 3.2.2, by increasing surface friction. In paper **VIII**, we studied spin-down-induced vortex flow in the lowermost volume of *setup 1* and in a cylinder without any division plates (*setup 2*). In both cases the vortex flow was perturbed at the bottom end of the sample tube by the presence of a rough and wavy sintered heat-exchanger surface.

In the experiments performed in *setup 1*, we studied how the vortex configuration created by a step change of the rotation velocity to rest affected the fraction Γ of thermal excitations returning to the bolometer volume described in Sec. 3.1.2. After bringing the container to rest, the heat $\dot{Q}_{\text{gen}}(T)$ generated in the bolometer at $T \approx 0.20T_{\text{c}}$, is the sum of the known background heat leak and the known heat release from the laminar decay of vortices stabilized by the mutual friction $\alpha \approx 0.002$ in the upper sections of the cylinder above the 0.3 mm orifice. The total heat flow out of the bolometer volume is given by

$$\dot{Q}(t) = \dot{Q}_{\text{gen}}(t) - c(T)V\dot{T}, \tag{3.8}$$

where $V = \pi R^2 h$ is the volume of the bolometer and the heat capacity $c(T)$ is given approximately by [90]

$$c(T) = k_B\sqrt{2\pi}N_F\left(\frac{\Delta}{k_BT}\right)^{\frac{3}{2}} e^{-\frac{\Delta}{k_BT}}\left(\Delta + \frac{21}{16}k_BT\right). \tag{3.9}$$

Here N_F is the density of states at the Fermi level. From the measured temperature and its time derivative $\dot{T}$ one can solve for the now time-dependent reflection coefficient $\Gamma(t)$ using Eqs. (3.8), (3.9), (3.3), and (3.4), where during the spin-down the effective area is a function of time instead of being a function of Ω.

Unlike in the case of a uniform vortex cluster in steady-state rotation (Sec. 3.1.2), during the spin-down the detailed structure of the vortex configuration below the 0.3 mm orifice was unknown. At a given vortex density L the amount of Andreev-reflected excitations is minimized if all the vortices are polarized along the axis of rotation. Thus, the upper limit for the vortex density at a given reflection coefficient could be obtained from the calibration measurements of Γ with known vortex density as described in Sec. 3.1.2. The lower limit could be estimated by considering a system of vortices perpendicular to the beam of excitations with an intervortex spacing $\ell = L^{-1/2}$ (see Sec. IV of paper **VIII** for details).

Figure 3.8 shows an example of the temperature response of the bolometer to a rapid spin-down to rest together with the lower-limit estimate for the vortex density L. The result for $L(t)$ carries the following characteristic signatures from turbulent flow: Firstly, an initial overshoot of the order of a few tens of percents indicates that part of the kinetic energy of the superfluid is converted to a turbulent tangle of vortices. The upper and lower limits of the maximum vortex density as a function of the initial rotation velocity are shown in the right panel of Fig. 3.9. The lower limit maximum lies close to the known initial density $2\Omega_{\text{ini}}/\kappa$. Secondly, after the overshoot the estimated vortex density fits well a $t^{-3/2}$ dependence on time. This suggests that at least some fraction of the vortices decayed in a turbulent manner, since for a fully laminar response the decay should have been proportional to t^{-1} as given by Eq. (3.6). In the left panel of Fig. 3.9, examples of the lower limit of the vortex density L at different initial rotation velocities are plotted on logarithmic scales illustrating the $t^{-3/2}$ time dependence.

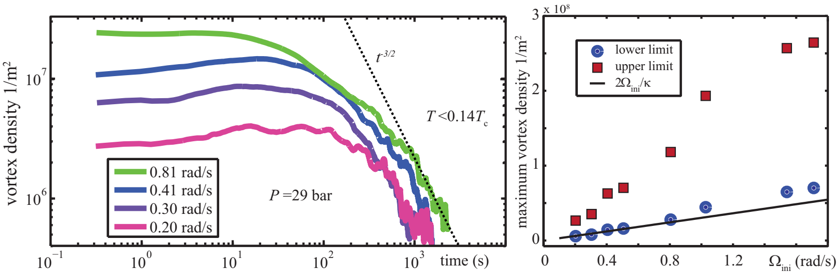

Fig. 3.9 (*Left*) Lower limit of the vortex density L as a function of time after bringing the container to rest for four initial velocities $\Omega_{\rm ini}$. A simple moving average filtering is used to reduce the noise in the data. The upper limit of L at each value of $\Omega_{\rm ini}$ obtained from a calibration measurement (Fig. 3.3) is a few times higher. (*Right*) Lower and upper limits for the maximum vortex density generated in spin-down soon after reaching $\Omega = 0$ together with the initial steady-state value $2\Omega_{\rm ini}/\kappa$.

It is tempting to relate the response in Fig. 3.9 with $t^{-3/2}$ time dependence to Eq. (1.7) for the quasiclassical decay of the line density. One needs to be careful though, since some of the assumptions leading to Eq. (1.7), especially the homogeneity of the flow, are not met. Nevertheless, if the size of the energy containing length scale is chosen to be the diameter of the container, i.e. $D = 2R$, the effective kinematic viscosity ν' extracted from the lower limit of vortex densities is $(1.0 \pm 0.3) \cdot 10^{-4}\kappa$ and the estimate obtained from the upper limit is roughly an order of magnitude smaller. The orders of magnitude smaller ν' in our experiment, compared to earlier experiments [81] with more homogeneous turbulence underlines the influence of the large polarization of vortices, which suppresses vortex reconnections and thus dissipation.

In *setup 2* the quartz tuning fork resonators located at the bottom of the cylinder could be used to probe the spin-down-induced flow field locally. In our experiments performed at 0.5 bar pressure, we studied the response of the superfluid to a rapid spin-down to rest by following the variation in the thermal excitation density in the vicinity of a tuning fork oscillator.

Figure 3.10 shows an example of the fork-oscillator response before, during, and after bringing the container to rest. The initial increase of the linewidth arose mainly from Andreev scattering from the turbulent vortex configuration generated in spin-down. After about 200 s, periodic oscillations were observed superimposed on the relaxing average temperature. These oscillations were interpreted to originate from a cluster of predominantly straight vortices precessing

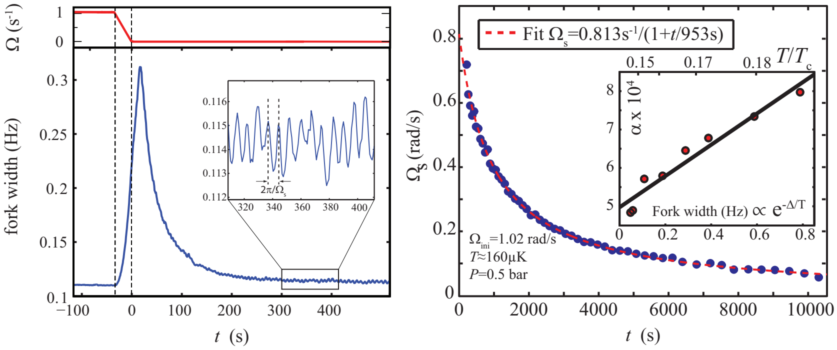

Fig. 3.10 (*Left*) Response of the linewidth of the quartz tuning fork oscillator to a rapid spin-down from $\Omega_{\rm ini}$=1.02 rad/s to rest. The initial increase arises mainly owing to Andreev reflection from the rapidly decaying turbulent vortex configuration generated in the early part of the spin-down. The inset shows the zoomed view of the oscillations in the laminar late response caused by a periodic variation of the thermal excitation density in the vicinity of the fork. These oscillations result from the Andreev scattering from an asymmetric vortex cluster precessing at angular velocity $\Omega_s(t)$. (*Right*) Superfluid angular velocity Ω_s as a function of time after bringing the container to rest at $t = 0$. The response fits perfectly to the laminar flow model [Eq. (3.6)] shown by the dashed line with $\Omega_0 \approx 0.80\Omega_{\rm ini}$ and $\alpha \approx 6.45 \cdot 10^{-4}$. The inset shows the dissipative mutual-friction parameter α as a function of the linewidth of the tuning fork oscillator (bottom axis) or temperature (top axis). The value of α, whose uncertainty is of order $\pm 5 \cdot 10^{-5}$, is extracted from the precession frequency of the vortex cluster as discussed in the text and averaged over 2-4 measurements at different rotation velocities in the range $\Omega_{\rm ini} = 0.6 - 1.5$ rad/s at the given temperature.

at the superfluid angular velocity Ω_s. A small asymmetry in the structure of the cluster caused periodic variation of the thermal excitation density in the vicinity of the tuning fork oscillator. The frequency of these oscillations was observed to drop as t^{-1} for several hours indicating the decay to be laminar. Using Ω_0 and τ as fitting parameters produces an excellent fit to Eq. (3.6) with $\Omega_0 = b\Omega_{\rm ini}$ and $\tau \propto \Omega_0^{-1}$, as expected for solid-body-like laminar decay (right panel of Fig. 3.10).

Both fitting parameters provided valuable information on the vortex dynamics during the spin-down. The rapid drop of the superfluid angular velocity from $\Omega_{\rm ini}$ to $\sim 0.8\Omega_{\rm ini}$ indicated that during the turbulent early part of the decay about one fifth of the vortices were annihilated. The initial turbulent part seemed to last a shorter time than in the measurements at 29 bar in Fig. 3.9. Two reasons for the increased turbulence in the high-pressure measurements could be given: At

0.5 bar pressure the vortex core radius is roughly five times larger than at 29 bar. Therefore, vortex pinning on the surface of the heat exchanger, which is sintered from $\sim$ 10-μm-size copper flakes, is expected to be stronger at high pressures. Second, the short narrow-diameter bottom part of the cylinder in *setup 1* is different from that of *setup 2*.

The two fitting parameters of the laminar decay allowed us to determine the mutual-friction parameter $\alpha = (2\tau\Omega_0)^{-1}$ down to temperatures below $0.15\,T_\mathrm{c}$, which corresponds to three orders of magnitude lower normal fluid densities than in the earlier measurements at low pressures [86]. The inset of the right panel of Fig. 3.10 demonstrates how α follows the expected exponential dependence on temperature, but with a nonzero intercept $\alpha(0) \sim 5 \cdot 10^{-4}$ in the $T \to 0$ limit. The source of this residual dissipation has not been explained. One possibility is surface interactions with the container walls. Another mechanism is local heating of the vortex cores in accelerating motion, which can lead to temperature-independent dissipation in the zero-temperature limit [43]. In Sec. 3.3 we discuss the zero-temperature dissipation observed in the turbulent vortex front propagation. Whether the origin of the finite value for α in our spin-down experiments is the same as in the front motion remains to be clarified.

3.3 Superfluid vortex front

The dynamics of vortices expanding in a rotating cylindrical container in ^{3}He-B to a region of vortex-free flow has been studied by the ROTA group for about ten years [91]. The procedure in these experiments is to first prepare the vortex-free state at constant container velocity Ω, then inject some vortices to the system, and follow what happens. In this work, the expansion dynamics was probed for the first time with thermal measurements and the experiments were extended to lower temperatures and wider range of rotation velocities than before.

At high temperatures, above $0.6\,T_\mathrm{c}$, the seed vortices expand along the container wall in laminar fashion approximately with the axial vortex-end velocity

$$\mathbf{v}_{\mathrm{L},z} = \alpha(T)\Omega R, \tag{3.10}$$

as obtained from Eq. 1.2, and the number of vortices is conserved [92]. At lower temperatures, where $\mathrm{Re}_\alpha > 1$, the injected vortices interact in a turbulent manner and create a large number of new vortices [93]. The transition temperature for the onset of bulk turbulence has not been found to depend on the rotation velocity [94], but depends on the seed-vortex configuration and on the strength of the flow perturbation [95].

The expanding vortices form a front, in which the ends of the vortex lines bend to the sidewall. The core of the front, with an axial length comparable to the cylinder radius R, rotates at a different speed than the growing bundle behind it and consequently, they both are twisted [96]. The propagation velocity V_f of the front remains close to the single-vortex velocity (3.10) down to $T \approx 0.45\,T_\mathrm{c}$, below which the turbulent processes provide extra dissipation, which makes the propagation faster than in Eq. (3.10) [38]. The front is one of the rare examples of steady-state turbulent motion in superfluid ^{3}He-B that can be studied in experiments in a wide temperature range including the $T \to 0$ limit.

In our recent work two vortex-injection methods were used to trigger the front motion. The first method used in the measurements in paper **V** relies on the so-called Kelvin-Helmholtz shear flow instability of the AB interface [97]. The barrier magnet in the middle of the top section of *setup 1* was used to stabilize a narrow A-phase layer at constant rotation velocity. At given Ω the AB interface becomes unstable at a temperature-dependent strength of the magnetic field and its gradient at the interface. Due to the instability event, a number of vortex loops escape across the AB interface from the A to the B phase. The loops interact and produce a large number of vortices in a turbulent burst close to the AB interface. The instability occurs simultaneously at the two AB interfaces in *setup 1*. Consequently, both upward- and downward-propagating fronts are set into motion. A significant asset of this method is that the rotation velocity can be kept constant, which was crucial for the thermal measurements in papers **V** and **X**.

Another method is to apply a large enough counterflow by increasing the rotation velocity slowly until the critical velocity for vortex formation is reached locally at some rough spot on the container boundary. The sintered-metal powder provides ideal nucleation points for vortices making the critical velocity for vortex formation rather low. Thus, in *setup 2*, where the cylinder directly opened to the heat-exchanger volume, the front motion upward to the cylinder could be started at very low rotation velocities. Owing to the high critical velocity Ω_c at the quartz cylinder walls, the volume above the front remained in the vortex-free Landau state which eventually was displaced by the front. In order to recreate the Landau state after injecting vortices into the system, the sample was warmed up to high temperatures, $0.7\,T_\mathrm{c}$ or above, to allow for fast annihilation of remanent vortices [98].

The front propagation was monitored with two NMR pick-up coils. At temperatures above $0.2\,T_\mathrm{c}$, the front could be detected by tracing the NMR signal at the counterflow peak. The arrival of the front was seen as a rapid decrease of the NMR absorption. At the lowest rotation velocity of our measurements,

$\Omega \approx 0.4$ rad/s, this detection method lost sensitivity at around $0.23\,T_\mathrm{c}$, especially for the coil at the top operating at a smaller value of steady magnetic field. Even at higher velocities, the counterflow peak became practically invisible below $0.18\,T_\mathrm{c}$. At lower temperatures, the front propagation could be monitored with the frequency shift of the magnon-condensate resonance [99], which originates from the textural trap in the middle of the pick-up coil with strong dependence on the amount of local counterflow.

3.3.1 Thermal signal from dissipation of turbulence in the vortex front

In papers **V** and **X** we used bolometric methods to directly measure the heat released during turbulent front motion. These were the first measurements on the thermal signal from the dissipation of vortex flow. [2]

The free-energy difference between the vortex-free superfluid and the state of equilibrium rotation is $\pi \rho_\mathrm{s} R^4 \Omega^2/4$ per unit length in the axial direction. Here the small correction due to the narrow vortex free annulus is neglected. The heat generated in a spin-up process where the vortex-free state is displaced by the front is equal to the change of free energy of the superfluid. In the simplest model all the dissipation is concentrated in the thin core of the front and the bundle behind the front contains the equilibrium number of vortices $2\Omega\pi R^2\kappa^{-1}$, i.e., the superfluid angular velocity in the bundle $\Omega_s \approx \Omega$. This gives the maximum possible rate of the heat release during the front motion as

$$\dot{Q} = \frac{\pi \rho_\mathrm{s}}{4} R^4 \Omega^2 V_f\,. \tag{3.11}$$

The thermal measurements were performed in *setup 1* at $0.20\,T_\mathrm{c}$ with the rotation velocity ranging from 0.8 to 1.2 rad/s. The front was triggered using the Kelvin-Helmholtz instability: either the current in the barrier magnet in Fig. 3.11 was decreased triggering the instability on the pre-existing AB interface, or increased creating an A phase slab with two unstable interfaces. The heat release could be measured from the temperature increase of the bolometer using Eq. (3.3) with known calibration for the effective area $A_h(\Omega)$. The sensitivity of the measurement was limited by the fluctuations of the heat leak at a level of ~ 0.1 pW on top of its mean value ~ 20 pW.

Fig. 3.11 shows examples of thermal measurements of the front propagation. The total integrated energy agrees with the calculated free-energy difference

---

[2] Shortly after our studies, the heat released in a free decay of turbulence was measured in Lancaster [100].

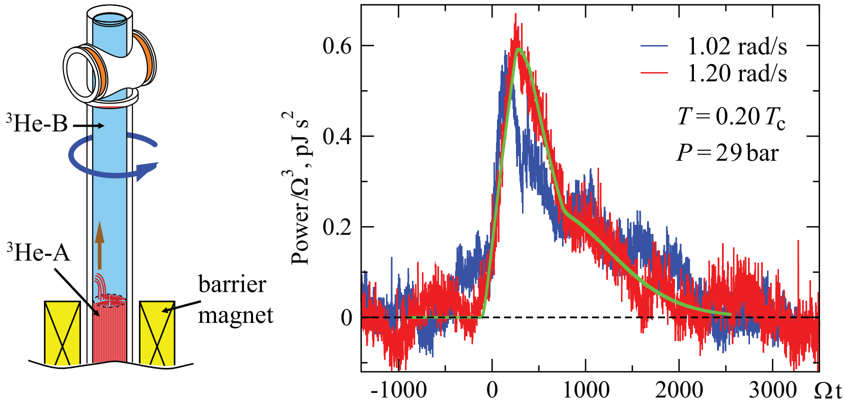

Fig. 3.11 (*Left*) Principle of the measurement. By manipulating the current in the barrier magnet in the middle of the sample the front motion could be triggered at constant rotation velocity Ω. The propagation was monitored with NMR pick-up coils. (*Right*) Two Ω-scaled bolometer signals with the background heat leak subtracted. Time $t = 0$ corresponds to the moment when the front motion was triggered. The green curve represents a fit to the experimental record at $\Omega = 1.2\,\text{rad/s}$.

within the uncertainties in the bolometer calibration. The maximum of the power signal corresponds to the time when the front arrives to the end of the sample. Surprisingly, most of the energy was released only after this moment. If the bundle behind the front would have corresponded to the steady-state of rotation with $\Omega_s \approx \Omega$, all the heat release should have happened during the front motion. Thus, the vortex configuration behind the front must have contained less than the equilibrium number vortices, and the late relaxation starting from the shoulder at $\Omega t \sim 1000$ must have originated from a slow laminar spin-up of the superfluid component. A simple model fitted to the thermal record at 1.2 rad/s (green curve), yielded that the turbulent front, with only 0.35 of the equilibrium number of vortices, was followed by laminar relaxation with a time constant of 500 s.

Often the vortex arrangement in the front and in the bundle behind it is not perfectly axially symmetric. This asymmetry was sometimes seen as oscillations in the NMR signal. The ratio of the precession period, which for solid-body-like rotation equals $2\pi/\Omega_s$, to $2\pi/\Omega$ is equal to the ratio of the vortex number in the bundle and the equilibrium array of vortices. The measured precession signal in Fig. 3.12 agrees in this respect with the thermal signal and also shows that the precession frequency of the front is roughly half of that of the bundle.

The observed deficit of vortices was also seen in the numerical simulations using

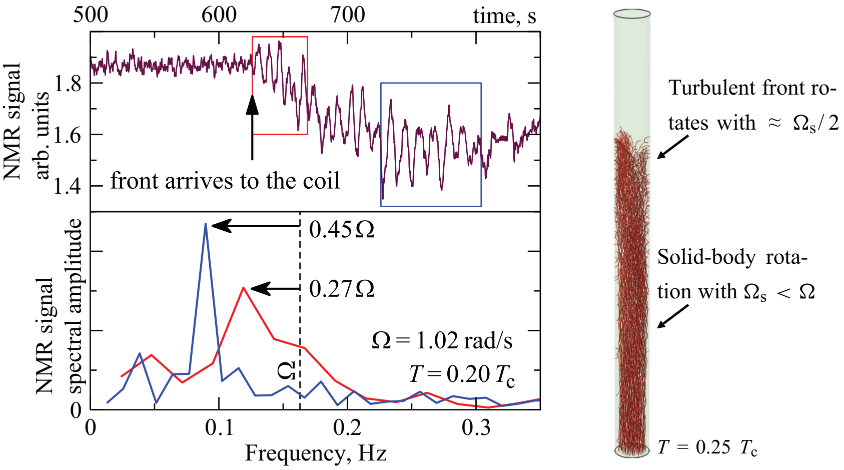

Fig. 3.12 Precession of the vortex front and the bundle behind it. (*Top*) Oscillations in the magnon-resonance NMR signal when the front arrives to the pick-up coil result from the precessing motion of vortices. (*Bottom*) Fourier transforms of parts of the NMR signal marked in the top panel: the front (red) and the cluster behind it (blue). Since the NMR coil is fixed to the rotating frame, the precession frequencies in the laboratory frame are counted relative to the angular velocity Ω, as shown by the arrows. (*Right*) Snapshot of the front motion from numerical simulations showing the turbulent front and the bundle behind with $\Omega_s < \Omega$.

the vortex-filament model. The simulations demonstrate that the vortex density behind the front stays constant as a function of the axial distance z, but the corresponding superfluid angular velocity Ω_s decreases significantly at temperatures below $0.3\,T_c$. This is demonstrated in Fig. 3.13 (upper panel) together with the number of reconnections supporting the turbulence in the front (lower panel). At $0.20\,T_c$, Ω_s from simulation calculations agrees well with the experiments.

The thermal measurements, the front precession signal, and the numerical simulations all indicate that the vortex state behind the turbulent core of the front corresponds to a solid-body-like quasiequilibrium state where the superfluid angular velocity $\Omega_s < \Omega$. Thus, the superfluid becomes effectively decoupled from the reference frame of the container as the source for the coupling, the mutual friction, decreases with decreasing temperature.

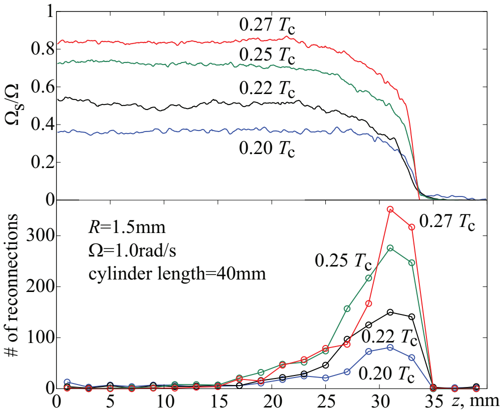

Fig. 3.13 Turbulent vortex front in numerical simulations. Snapshots of vortex configurations at different temperatures are analyzed when the front is located at the same axial position $z = 34$ mm. *(Top)* The normalized superfluid angular velocity Ω_s as a function of z showing the vortex-free state before the front ($z > 35$ mm) and the quasi-equilibrium vortex state with $\Omega_\mathrm{s}(T) < \Omega$ behind the front. *(Bottom)* Number of vortex reconnections, which have been counted here within bins of width $\Delta z = 2$ mm over a time interval in which the front propagates 0.5 mm. The reconnections, which support the steady-state turbulent motion, are caused by the differential rotation of the front with respect to the bundle behind it and are concentrated in the core of the front.

3.3.2 Front propagation in a decoupled superfluid

The decoupling of the superfluid from the container reference frame at low temperatures can be understood on the basis of two competing forces exerted on the superfluid, the mutual-friction force

$$\mathbf{F}_\alpha = -\alpha\hat{\omega} \times ((\mathbf{v}_\mathrm{s} - \mathbf{v}_\mathrm{n}) \times (\nabla \times \mathbf{v}_\mathrm{s}))\,, \tag{3.12}$$

and the force due to line tension [101],

$$\mathbf{F}_\lambda = -\lambda(\nabla \times \mathbf{v}_\mathrm{s}) \times (\nabla \times \hat{\omega})\,. \tag{3.13}$$

The line tension parameter λ is given by

$$\lambda = (\kappa/4\pi)\ln(\ell/a). \tag{3.14}$$

In equilibrium, with the vortex configuration behind the front in solid-body rotation, the global force balance dictates $\langle F_\alpha \rangle = \langle F_\lambda \rangle$ for the azimuthal components

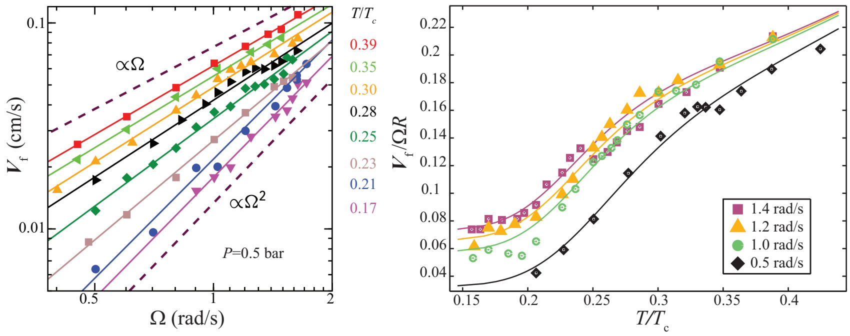

Fig. 3.14 Measured vortex front velocity. The left panel shows the front velocity V_f as a function of rotation velocity Ω at eight different temperatures in the range 0.17-0.39 T_c and the right panel the scaled front velocity $V_f/\Omega R$ as a function of temperature at four different rotation velocities. The solid lines represent the velocity fitted to Eq. (3.17) with the fitting parameters obtained from a common fit to all the data in both figures.

F_α and F_λ of $\mathbf{F}_\alpha$ and $\mathbf{F}_\lambda$. The approximation for the superfluid angular velocity can be written as **IX**

$$\Omega_s = \frac{\alpha_{\rm am}}{\alpha_{\rm am}\Omega + \lambda R^{-2}}\Omega^2, \tag{3.15}$$

where $\alpha_{\rm am}$ is the mutual friction parameter for angular momentum given by

$$\alpha_{\rm am} = C_{\rm am}\alpha(T) + \alpha_{\rm res}. \tag{3.16}$$

Here $C_{\rm am}$ is a constant of the order of unity and the constant $\alpha_{\rm res}$ accounts for all the residual effects related to angular momentum transfer, such as vortex pinning or friction on the container walls. Requiring global energy balance [**IX**], the front velocity is given by

$$V_f \approx \alpha_{\rm eff}(T)\Omega_s R = (C\alpha + \alpha_{\rm turb})\frac{C_{\rm am}\alpha + \alpha_{\rm res}}{(C_{\rm am}\alpha + \alpha_{\rm res})\Omega + \lambda R^{-2}}\Omega^2 R, \tag{3.17}$$

where the constant C of the order of unity and the constant $\alpha_{\rm turb}$ account for the energy transfer, and thus dissipation, due to the turbulent cascade.

In paper **IX** we presented extensive studies on the front propagation velocity both as a function of temperature and as a function of rotation velocity. The measurements were performed in *setup* 2, where the front was triggered with a rapid increase of Ω from rest to the target velocity in the range $0.4 - 1.7$ rad/s.

According to Eq. (3.17), the front velocity should be proportional to Ω in the mutual-friction dominated high-temperature limit, whereas with decreasing mutual friction, the dependence should tend to Ω^2 dependence. This is seen in our measurements, as shown in the left panel of Fig. 3.14. The right panel of the figure shows the scaled velocity $v_f = V_f/\Omega R$ as a function of temperature at four different rotation velocities. All the measurements were fit to Eq. (3.17) using C, C_{am}, α_{turb}, and α_{res} as common fitting parameters yielding $C \approx 0.5$, $C_{\mathrm{am}} \approx 1.3$, $\alpha_{\mathrm{turb}} \approx 0.20$, and $\alpha_{\mathrm{res}} \approx 0.002$. All the data can be fit in a satisfactory manner, as shown by the solid lines in Fig. 3.14.

The model agrees well with the measurements in a wide region of angular velocities (0.3–1.7 rad/s) and temperatures (from $0.17\,T_{\mathrm{c}}$ to $\sim 0.4\,T_{\mathrm{c}}$), where the main physical parameter of the problem, the mutual friction parameter α, varies by three orders of magnitude. The model does not include the small unexpected variations at intermediate temperatures $0.25 < T/T_{\mathrm{c}} < 0.35$. The left panel of Fig. 3.15 shows a zoomed view of the Ω-dependence at temperatures 0.28 and $0.30\,T_{\mathrm{c}}$, where v_f is nonmonotonous with a temperature-dependent maximum at Ω=1-1.2 rad/s. The right panel contains a zoomed view of the temperature dependence for two different rotation velocities showing plateaus at rotation-velocity-dependent temperatures. These features have remained unexplained so far, but they might be accounted for by the bottleneck accumulation of the kinetic energy that was earlier used to explain the temperature dependence of the front velocity at intermediate temperatures [38, 40, 102]. The bottleneck scheme is supported by the fact that the value of the mutual-friction parameter corresponding to the plateaus decreases with increasing rotation velocity. The bottleneck would lead to a complex Ω- and T-dependence of the parameter α_{turb} which is responsible for the turbulent energy dissipation in the system. In the model (Eq. 3.17) all the fitting parameters are assumed to be temperature and rotation-velocity independent for simplicity. It remains as an interesting challenge to develop a detailed model of the front propagation which combines the decoupling with the complicated turbulence-induced processes and also includes the bottleneck scheme.

The residual term of the angular-momentum transfer α_{res} is about four times larger but still comparable to the corresponding residual term observed for laminar vortex motion in Sec. 3.2.3. The larger value is expected, since it reflects the additional residual processes induced by the turbulence in the front such as vortex reconnections, which are not present in the case of laminar motion. Remarkably, α_{res} is still a factor of hundred smaller than the residual term α_{turb} describing the energy transfer in the turbulent energy cascade. This means that the turbulent processes effectively compensate for the vanishing mutual friction in terms of the energy transfer and consequently, the front velocity becomes practically temperature independent at temperatures below $0.2\,T_{\mathrm{c}}$. The angular momentum transfer, however, is not efficiently compensated. This leads to the

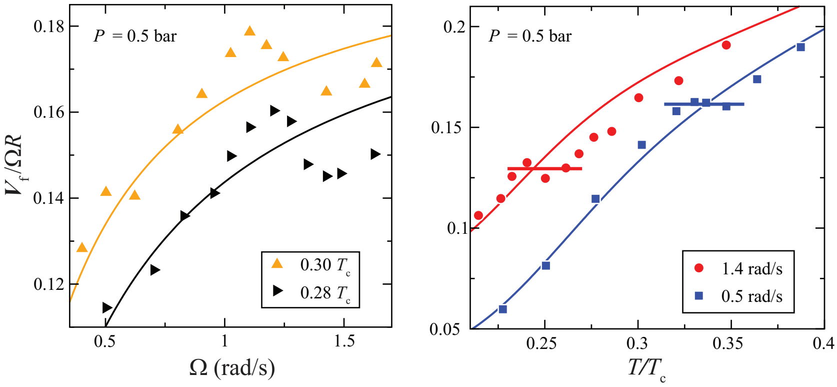

Fig. 3.15 Nonmonotonous features in the front velocity. The left panel shows a zoomed view of the nonmonotonous scaled front velocity $v_f = V_f/\Omega R$ at temperatures 0.28 and 0.30 T_c illustrating maxima at Ω=1-1.2 rad/s. On the right is a zoomed view of the temperature dependence for two different rotation velocities showing plateaus at rotation-velocity-dependent temperatures. The solid lines show the velocity from Eq. (3.17) with the fitting parameters given in the text.

observed quasiequilibrium solid-body-like rotation with $\Omega_s < \Omega$ for the vortex state behind the front.

Chapter 4

Summary and conclusions

The measurements of this thesis present the first and only information on the interplay of laminar and turbulent vortex-flow responses and the associated dissipation in coherent quantum systems in the zero-temperature limit. Before this work the general belief appeared to be that in the limit of vanishing mutual friction, vortex flow inevitably tends to become turbulent. Now we find that the zero-temperature dissipation mechanisms are more complicated and diverse than originally expected. Practically all the experiments confirm that some dissipative processes exist even in the limit of vanishing normal-excitation density. This was known before for turbulent vortex flow, but here it has been found to apply also to laminar motion in the bulk volume, in the absence of vortex reconnections.

The thesis focuses on the dissipation of the superfluid motion at ultralow temperatures, where the normal-fluid density approaches zero. The measurements in papers **III**, **IV**, **VI**, and **VIII** concentrated on the response of the superfluid to a sudden change of the rotation velocity of the container. Vortex reconnections were found to play a crucial role in the dissipation and in the nature of the flow in the $T \to 0$ limit. In a smooth-walled cylinder, the vortex-flow response in ^{3}He-B was found to remain laminar even in the limit of vanishing normal fluid fraction. This fact was deduced from the NMR signature of the decaying superfluid counterflow. As was shown in papers **III** and **IV** in NMR measurements and numerical simulations, the characteristic feature of the laminar flow is a low incidence of reconnections and of Kelvin-wave excitations in the bulk volume. With increasing surface friction, the flow response was found to become turbulent. In paper **VI** the surface friction on the B-phase vortex ends was changed by replacing the solid end plate of the cylinder with the interface of two superfluids, ^{3}He-B and ^{3}He-A. These two phases display vastly different time scales of vortex flow which leads to a large effective surface friction for the B-phase vortices. The NMR measurements and numerical simulations showed how turbulence close to the AB interface brings about increased dissipation and thus, a faster response.

The spin-down response of superfluid ^{3}He-B in a cylindrical container at very low temperatures, when the normal fluid excitations are extremely dilute, was studied in paper **VIII**. The low mutual friction together with small deviations from an ideal axially-symmetric flow environment was found to result in turbulent flow. Similarly to increased surface friction, the increased vortex pinning on the rough and wavy heat-exchanger surface was shown to lead to increased turbulence. The vortex core size was found to affect the decay, which agrees with the conclusion that vortex pinning plays a role in maintaining turbulent flow. The high polarization of the vortices along the rotation axis was demonstrated to significantly suppress the effective turbulent kinematic viscosity ν' below the values reported for more homogeneous turbulence and was shown to lead to a laminar late-time response.

The vortex density in the late spin-down decay was inferred with high accuracy from the local temperature variations caused by Andreev reflection from the precessing slightly asymmetric cluster of quantized vortex lines. This novel method revealed that the late decay of the vortex cluster remains laminar even at the lowest temperatures. The temporal dependence of the spin-down decay allowed us to determine both the amount of vortices lost in the initial turbulent part of the decay and the vortex mutual friction down to much lower normal fluid densities than before. The dissipative mutual friction parameter α was found to approach a small nonzero value in the low temperature limit. This was the first time this type of residual friction was observed for laminar motion.

Along with the traditional NMR methods, the quartz-tuning-fork oscillators were proven to be useful tools for studying quantum liquids. In papers **I** and **II**, the forks were shown to be able to act not only as pressure-, visco-, and thermometers in helium liquids, but also as generators and detectors of quantum turbulence. Thereafter, the forks have become popular probes of both superfluid ^{3}He and ^{4}He. We used them for thermometry in all the experiments described in this thesis.

In paper **VII** the forks were used in the first measurement of Andreev reflection of thermal excitations from a well-defined configuration of quantized vortices, and the results were reproduced by our numerical simulations with a good accuracy. This work provides a rigorous quantitative basis for the use and further development of the quasiparticle-beam techniques for direct visualization purposes.

The spin-up of the superfluid from the metastable vortex-free state in the form of a propagating superfluid front was studied extensively in papers **V**, **IX**, and **X**. The thermal measurements of the front motion provided the first direct observation of the quasiparticle excitations created in both turbulent and laminar vortex flow. These measurements of the heat release and the measurements of the precession frequency of the vortices together with numerical simulations indicated that the superfluid gradually decouples from the reference frame of the container with decreasing temperature. The measurements of the front velocity revealed that the reconnection-driven turbulent flow in the front leads to temperature-independent but rotation-velocity-dependent dissipation in the limit $T \to 0$. The decoupling and the main features of the velocity measurements were explained by a phenomenological model, which in addition to the mutual friction takes into account the line tension in the presence of a nonuniform precession frequency in the turbulent vortex structure.

To understand the flow dynamics on approaching the zero-temperature limit, phenomena both at large and microscopic length scales need to be known. These include the energy and angular-momentum transfer in turbulence, the role of Kelvin-waves, vortex pinning, and surface interactions, and the emission of vortex-core-bound excitations. A detailed theory of superfluid hydrodynamics in the zero-temperature limit is still in the making, but our experiments have provided new and unexpected input for this work.

References

[1] L. Onsager, Nuovo Cimento Suppl. **6**, 249 (1949).

[2] R. P. Feynman, in *Progress in Low Temperature Physics*, edited by C. J. Gorter (North Holland Publishing Co., Amsterdam, 1956), vol. I, p. 17.

[3] W. F. Vinen, Nature **181**, 1524 (1958).

[4] P. J. Hakonen, O. T. Ikkala, S. T. Islander, O. V. Lounasmaa, T. K. Markkula, P. Roubeau, K. M. Saloheimo, G. E. Volovik, E. L. Andronikashvili, D. I. Garibashvili, et al., Phys. Rev. Lett. **48**, 1838 (1982).

[5] P. J. Hakonen, O. T. Ikkala, and S. T. Islander, Phys. Rev. Lett. **49**, 1258 (1982).

[6] A. J. Leggett, Rev. Mod. Phys. **47**, 331 (1975).

[7] J. C. Wheatley, Rev. Mod. Phys. **47**, 415 (1975).

[8] D. Vollhardt and P. Wölfle, *The Superfluid Phases of Helium 3* (Taylor and Francis, London, 1990).

[9] E. R. Dobbs, *Helium three* (Oxford University Press, Oxford, 2000).

[10] F. Pobell, *Matter and Methods at Low Temperatures* (Springer-Verlag, Berlin, 1992), 1st ed.

[11] M. H. Anderson, J. R. Ensher, M. R. Matthew, C. E. Wieman, and E. A. Cornell, Science **269**, 198 (1995).

[12] K. B. Davis, M. O. Mewes, M. R. Andrews, N. J. van Druten, D. S. Durfee, D. M. Kurn, and W. Ketterle, Phys. Rev. Lett. **75**, 3969 (1995).

[13] D. R. Tilley and J. Tilley, *Superfluidity and Superconductivity* (IOP Publishing Ltd, Bristol, 1990), 3rd ed.

[14] J. Bardeen, L. N. Cooper, and J. R. Schrieffer, Phys. Rev. **108**, 1175 (1957).

[15] G. E. Volovik, *The Universe in a Helium Droplet* (Clarendon Press, Oxford, UK, 2003).

[16] L. D. Landau, Zh. Eksp. Teor. Fiz. **30**, 1058 (1956).

[17] W. F. Brinkman, J. W. Serene, and P. W. Anderson, Phys. Rev. A **10**, 2386 (1974).

[18] J. Kopu, R. Schanen, R. Blaauwgeers, V. B. Eltsov, M. Krusius, J. J. Ruohio, and E. V. Thuneberg, J. Low Temp. Phys. **120**, 213 (2000).

[19] E. M. Lifshitz and L. P. Pitaevskii, *Statistical Physics, Part 2* (Pergamon Press, Oxford, UK, 1980).

[20] O. V. Lounasmaa and E. V. Thuneberg, Proc. Natl. Acad. Sci. USA **96**, 7760 (1999).

[21] E. V. Thuneberg, Phys. Rev. Lett. **56**, 359 (1986).

[22] H. E. Hall and W. Vinen, Proc. R. Soc. A **238**, 204 (1956).

[23] H. E. Hall and W. Vinen, Proc. R. Soc. A **238**, 215 (1956).

[24] R. J. Donnelly, *Quantized Vortices in Helium II* (Cambridge University Press, Cambridge, 1991).

[25] N. B. Kopnin, Rep. Prog. Phys. **65**, 1633 (2002).

[26] M. Tinkham, *Introduction to Superconductivity* (Dover Publications, Inc., Mineola, New York, 2004), 2nd ed.

[27] M. Krusius, J. S. Korhonen, Y. Kondo, and E. B. Sonin, Phys. Rev. B **47**, 15113 (1993).

[28] L. D. Landau and E. M. Lifshitz, *Fluid mechanics* (Pergamon Press, Oxford, UK, 1987), 2nd ed.

[29] E. B. Sonin, Rev. Mod. Phys. **59**, 87 (1987).

[30] P. M. Walmsley, A. I. Golov, H. E. Hall, A. A. Levchenko, and W. F. Vinen, Phys. Rev. Lett. **99**, 265302 (2007).

[31] M. S. Paoletti, M. E. Fisher, K. R. Sreenivasan, and D. P. Lathrop, Phys. Rev. Lett. **101**, 154501 (2008).

[32] L. Skrbek and W. F. Vinen, in *Progress in Low Temperature Physics*, edited by M. Tsubota and W. Halperin (Elsevier B.V., Amsterdam, 2009), vol. XVI, p. 195.

[33] S. N. Fisher and G. R. Pickett, in *Progress in Low Temperature Physics*, edited by M. Tsubota and W. P. Halperin (Elsevier B.V., Amsterdam, 2009), vol. XVI, p. 147.

[34] W. F. Vinen, J. Low Temp. Phys. **161**, 419 (2010).

[35] S. R. Stalp, L. Skrbek, and R. J. Donnelly, Phys. Rev. Lett. **82**, 4831 (1999).

[36] G. E. Volovik, J. Low Temp. Phys. **136**, 309 (2004).

[37] P. M. Walmsley and A. I. Golov, Phys. Rev. Lett. **100**, 245301 (2008).

[38] V. B. Eltsov, A. I. Golov, R. de Graaf, R. Hänninen, M. Krusius, V. S. L'vov, and R. E. Solntsev, Phys. Rev. Lett. **99**, 265301 (2007).

[39] E. Kozik and B. Svistunov, Phys. Rev. Lett. **100**, 195302 (2008).

[40] V. S. L'vov, S. V. Nazarenko, and O. Rudenko, Phys. Rev. B **76**, 024520 (2007).

[41] E. B. Sonin, Phys. Rev. B **85**, 104516 (2012).

[42] W. F. Vinen, Phys. Rev. B **64**, 134520 (2001).

[43] M. A. Silaev, Phys. Rev. Lett. **108**, 045303 (2012).

[44] R. Blaauwgeers, Ph.D. thesis, Helsinki University of Technology (2002).

[45] R. Blaauwgeers, S. Boldarev, V. B. Eltsov, A. P. Finne, and M. Krusius, J. Low Temp. Phys. **132**, 263 (2003).

[46] R. J. de Graaf, Ph.D. thesis, Aalto University (2011).

[47] A. M. Guénault, V. Keith, C. J. Kennedy, S. G. Mussett, and G. Pickett, J. Low Temp. Phys. **62**, 511 (1986).

[48] D. O. Clubb, O. V. L. Buu, R. M. Bowley, R. Nyman, and J. R. Owers-Bradley, J. Low Temp. Phys. **136**, 1 (2004).

[49] M. Blažková, D. Schmoranzer, L. Skrbek, and W. F. Vinen, Phys. Rev. B **79**, 054522 (2009).

[50] M. Blažková, M. Človečko, E. Gažo, L. Skrbek, and P. Skyba, J. Low Temp. Phys. **148**, 305 (2007).

[51] G. Sheshin, A. A. Zadorozhko, E. Rudavskii, V. Chagovets, L. Skrbek, and M. Blažková, Low Temp. Phys. **34**, 875 (2008).

[52] D. I. Bradley, M. J. Fear, S. N. Fisher, A. M. Guénault, R. P. Haley, C. R. Lawson, P. V. E. McClintock, G. R. Pickett, R. Schanen, V. Tsepelin, et al., J. Low Temp. Phys. **156**, 116 (2009).

[53] D. I. Bradley, P. Crookston, S. N. Fisher, A. Ganshin, A. M. Guénault, R. P. Haley, M. J. Jackson, G. R. Pickett, R. Schanen, and V. Tsepelin, J. Low Temp. Phys. **157**, 476 (2009).

[54] D. Garg, V. B. Efimov, M. Giltrow, P. V. E. McClintock, L. Skrbek, and W. F. Vinen, Phys. Rev. B **85**, 144518 (2012).

[55] M. Blažková, D. Schmoranzer, and L. Skrbek, Phys. Rev. E **75**, 025302 (2007).

[56] D. Schmoranzer, M. Král'ová, V. Pilcová, W. F. Vinen, and L. Skrbek, Phys. Rev. E **81**, 066316 (2010).

[57] P. Skyba, J. Low Temp. Phys. **160**, 219 (2010).

[58] J.-M. Friedt and É. Carry, Am. J. Phys. **75**, 415 (2007).

[59] R. J. Donnelly and C. F. Barenghi, J. Phys. Chem. Ref. Data **27**, 1217 (1998).

[60] C. B. Winkelmann, E. Collin, Y. M. Bunkov, and H. Godfrin, J. Low Temp. Phys. **135**, 3 (2004).

[61] S. N. Fisher, A. M. Guénault, C. J. Kennedy, and G. R. Pickett, Phys. Rev. Lett. **67**, 1270 (1991).

[62] D. I. Bradley, M. Človečko, E. Gažo, and P. Skyba, J. Low Temp. Phys. **151**, 147 (2008).

[63] D. Rainer and J. W. Serene, Phys. Rev. B **13**, 4745 (1976).

[64] D. S. Greywall, Phys. Rev. B **33**, 7520 (1986).

[65] I. A. Todoschenko, H. Alles, A. Babkin, A. Y. Parshin, and V. Tsepelin, J. Low Temp. Phys. **126**, 1446 (2002).

[66] D. S. Greywall and P. A. Busch, J. Low Temp. Phys. **46**, 451 (1982).

[67] D. S. Greywall, Phys. Rev. B **31**, 2675 (1985).

[68] P. J. Hakonen, M. Krusius, M. M. Salomaa, R. H. Salmelin, J. T. Simola, A. D. Gongadze, G. E. Vachnadze, and G. A. Kharadze, J. Low Temp. Phys. **76**, 225 (1989).

[69] P. Sclichter, *Principles of magnetic resonance* (Springer-Verlag, Berlin, 1978).

[70] A. J. Leggett, Ann. Phys. (USA) **85**, 11 (1974).

[71] A. I. Ahonen, M. Krusius, and M. Paalanen, J. Low Temp. Phys. **25**, 421 (1976).

[72] J. S. Korhonen, A. D. Gongadze, Z. Janú, Y. Kondo, M. Krusius, Y. M. Mukharsky, and E. V. Thuneberg, Phys. Rev. Lett. **65**, 1211 (1990).

[73] V. Ruutu, Ü. Parts, J. Koivuniemi, N. Kopnin, and M. Krusius, Journal of Low Temperature Physics **107**, 93 (1997).

[74] A. F. Andreev, Zh. Eksp. Teor. Fiz. **46**, 1823 (1964).

[75] C. F. Barenghi, Y. A. Sergeev, and N. Suramlishvili, Phys. Rev. B **77**, 104512 (2008).

[76] P. Wölfle, Rep. Prog. Phys. **42**, 269 (1979).

[77] S. N. Fisher, A. M. Guénault, C. J. Kennedy, and G. R. Pickett, Phys. Rev. Lett. **63**, 2566 (1989).

[78] C. F. Barenghi, Y. A. Sergeev, N. Suramlishvili, and P. J. van Dijk, Phys. Rev. B **79**, 024508 (2009).

[79] D. I. Bradley, S. N. Fisher, A. M. Guénault, M. R. Lowe, G. R. Pickett, A. Rahm, and R. C. V. Whitehead, Phys. Rev. Lett. **93**, 235302 (2004).

[80] D. I. Bradley, D. O. Clubb, S. N. Fisher, A. M. Guénault, R. P. Haley, C. J. Matthews, G. R. Pickett, V. Tsepelin, and K. Zaki, Phys. Rev. Lett. **95**, 035302 (2005).

[81] D. I. Bradley, D. O. Clubb, S. N. Fisher, A. M. Guénault, R. P. Haley, C. J. Matthews, G. R. Pickett, V. Tsepelin, and K. Zaki, Phys. Rev. Lett. **96**, 035301 (2006).

[82] D. I. Bradley, S. N. Fisher, A. M. Guénault, R. P. Haley, S. O'Sullivan, G. R. Pickett, and V. Tsepelin, Phys. Rev. Lett. **101**, 065302 (2008).

[83] S. N. Fisher, A. J. Hale, A. M. Guénault, and G. R. Pickett, Phys. Rev. Lett. **86**, 244 (2001).

[84] A. M. Guénault and G. R. Pickett, Physica (Amsterdam) **126B**, 260 (1984).

[85] D. M. Mathis and G. P. Neitzel, Phys. Fluids **28**, 449 (1985).

[86] T. D. C. Bevan, A. J. Manninen, J. B. Cook, A. J. Armstrong, J. R. Hook, and H. E. Hall, Phys. Rev. Lett. **74**, 750 (1995).

[87] T. D. C. Bevan, A. J. Manninen, J. B. Cook, H. Alles, J. R. Hook, and H. E. Hall, J. Low Temp. Phys. **109**, 423 (1997).

[88] R. de Graaf, V. B. Eltsov, P. J. Heikkinen, J. J. Hosio, and M. Krusius, J. Low Temp. Phys. **163**, 238 (2011).

[89] J. Kopu, J. Low Temp. Phys. **146**, 47 (2007).

[90] C. Bäuerle, Y. M. Bunkov, S. N. Fisher, and H. Godfrin, Phys. Rev. B **57**, 14381 (1998).

[91] V. B. Eltsov, R. de Graaf, R. Hänninen, M. Krusius, R. E. Solntsev, V. S. L'vov, A. I. Golov, and P. Walmsley, Prog. Low Temp. Phys. **XVI**, 45 (2009).

[92] A. P. Finne, V. B. Eltsov, R. Blaauwgeers, Z. Janu, M. Krusius, and L. Skrbek, Journal of Low Temperature Physics **134**, 375 (2004).

[93] A. P. Finne, T. Araki, R. Blaauwgeers, V. B. Eltsov, N. B. Kopnin, M. Krusius, L. Skrbek, M. Tsubota, and G. E. Volovik, Nature **424**, 1022 (2003).

[94] A. P. Finne, V. B. Eltsov, R. Blaauwgeers, Z. Janu, M. Krusius, and L. Skrbek, J. Low Temp. Phys. **138**, 567 (2005).

[95] A. P. Finne, V. B. Eltsov, G. Eska, R. Hänninen, J. Kopu, M. Krusius, E. V. Thuneberg, and M. Tsubota, Phys. Rev. Lett. **96**, 085301 (2006).

[96] V. B. Eltsov, A. P. Finne, R. Hänninen, J. Kopu, M. Krusius, M. Tsubota, and E. V. Thuneberg, Phys. Rev. Lett. **96**, 215302 (2006).

[97] R. Blaauwgeers, V. B. Eltsov, G. Eska, A. P. Finne, R. P. Haley, M. Krusius, J. J. Ruohio, L. Skrbek, and G. E. Volovik, Phys. Rev. Lett. **89**, 155301 (2002).

[98] R. E. Solntsev, R. de Graaf, V. B. Eltsov, R. Hänninen, and M. Krusius, J. Low Temp. Phys. **148**, 311 (2007).

[99] S. Autti, Y. M. Bunkov, V. B. Eltsov, P. J. Heikkinen, J. J. Hosio, P. Hunger, M. Krusius, and G. E. Volovik, Phys. Rev. Lett. **108**, 145303 (2012).

[100] D. I. Bradley, S. N. Fisher, A. M. Guénault, R. P. Haley, G. R. Pickett, D. Potts, and V. Tsepelin, Nature Phys. **7**, 473 (2011).

[101] R. Ostermeyer and W. Glaberson, J. Low Temp. Phys. **21**, 191 (1975).

[102] V. S. L'vov, S. V. Nazarenko, and O. Rudenko, J. Low Temp. Phys. **153**, 140 (2008).

Turbulence in viscous fluids has been studied for more than a century because of its pervading importance in many fields of science and technology. Turbulence in superfluids has been known for half a century, but quantum turbulence, the form it takes in the zero-temperature limit when the density of normal excitations approaches zero, has been in the forefront of research only during the last decade. This Ph.D. thesis describes measurements on the interplay of turbulent and laminar flow of quantized vortices in superfluid He-3 at temperatures down to 140 microkelvin in a rotating refrigerator. Motion in the zero-temperature limit turns out to be quite different and much more varied than was expected on the basis of high-temperature extrapolations.

ISBN 978-952-60-4849-9
ISBN 978-952-60-4850-5 (pdf)
ISSN-L 1799-4934
ISSN 1799-4934
ISSN 1799-4942 (pdf)

Aalto University
School of Science
O.V. Lounasmaa laboratory
www.aalto.fi

BUSINESS +
ECONOMY

ART +
DESIGN +
ARCHITECTURE

SCIENCE +
TECHNOLOGY

CROSSOVER

DOCTORAL
DISSERTATIONS